Estimating geodynamic model parameters from geodetic observations using a particle method

Marsman, C. P.; Vossepoel, F. C.; Van Dinther, Y.; Govers, R.

DOI
10.1093/gji/ggad450

Publication date
2024

Document Version
Final published version

Published in
Geophysical Journal International

Citation (APA)
Marsman, C. P., Vossepoel, F. C., Van Dinther, Y., & Govers, R. (2024). Estimating geodynamic model parameters from geodetic observations using a particle method. *Geophysical Journal International*, *236*(3), 1183-1205. https://doi.org/10.1093/gji/ggad450

Geophysical Journal International

Geophys. J. Int. (2024) **236,** 1183–1205
Advance Access publication 2023 December 6
GJI Geodynamics and Tectonics

https://doi.org/10.1093/gji/ggad450

Estimating geodynamic model parameters from geodetic observations using a particle method

C.P. Marsman [1], F.C. Vossepoel [2], Y. van Dinther [1] and R. Govers [1]

[1] *Department of Earth Sciences, Utrecht University, Princetonlaan* 4, 3584 *CB Utrecht, the Netherlands. E-mail: c.p.marsman@uu.nl*
[2] *Department of Geoscience and Engineering, Delft University of Technology, Stevinweg* 1, 2628 *CN Delft, the Netherlands*

Accepted 2023 November 15. Received 2023 October 25; in original form 2022 August 5

SUMMARY

Bayesian-based data assimilation methods integrate observational data into geophysical forward models to obtain the temporal evolution of an improved state vector, including its uncertainties. We explore the potential of a variant, a particle method, to estimate mechanical parameters of the overriding plate during the interseismic period. Here we assimilate vertical surface displacements into an elementary flexural model to estimate the elastic thickness of the overriding plate, and the locations and magnitudes of line loads acting on the overriding plate to produce flexure. Assimilation of synthetic observations sampled from a different forward model than is used in the particle method, reveal that synthetic seafloor data within 150 km from the trench are required to properly constrain parameters for long wavelength solutions of the upper plate (i.e. wavelength ∼500 km). Assimilation of synthetic observations sampled from the same flexural model used in the particle method shows remarkable convergence towards the true parameters with synthetic on-land data only for short to intermediate wavelength solutions (i.e. wavelengths between ∼100 and 300 km). In real-data assimilation experiments we assign representation errors due to discrepancies between our incorrect or incomplete physical model and the data. When assimilating continental data prior to the 2011 M_w Tohoku-Oki earthquake (1997–2000), an unrealistically low effective elastic plate thickness for Tohoku of ∼5–7 km is estimated. Our synthetic experiments suggest that improvements to the physical forward model, such as the inclusion of a slab, a megathrust interface and viscoelasticity of the mantle, including accurate seafloor data, and additional geodetic observations, may refine our estimates of the effective elastic plate thickness. Overall, we demonstrate the potential of using the particle method to constrain geodynamic parameters by providing constraints on parameters and corresponding uncertainty values. Using the particle method, we provide insights into the data network sensitivity and identify parameter trade-offs.

Key words: Inverse theory; Probabilistic forecasting; Statistical methods; Time-series analysis; Lithospheric flexure; Subduction zone processes.

1 INTRODUCTION

Measurements of surface deformation have evolved rapidly in precision, temporal and spatial resolution and global coverage with the introduction of space-based methods, such as continuous Global Navigation Satellite System (GNSS) and interferometric synthetic aperture radar (InSAR) observations. Advanced continuous geodetic networks are being used across tectonically active regions, such as the GNSS Earth Observation Network System (GEONET) in Japan (Sagiya *et al.*2000; Sagiya 2004) and the SCIGN network in Southern California (Bock *et al.*1997). The utilization of space geodetic observations has revolutionized our understanding of tectonic and seismic processes associated with the earthquake cycle over a broad range of spatial and temporal scales (e.g. Avouac 2015).

The observed crustal displacements reflect a superposition of tectonic processes and geodynamic models can help us to understand the driving forces of deformation. Models are continuously improved with faster computers and algorithms with lower computational cost, and by incorporating more (detailed) physical processes (Cohen 1999; Avouac 2015; Gerya 2022). However, the detailed implementation of physical processes in the model is not always clear from the literature. It is common practice in numerical model studies to vary parameters one-by-one within their uncertainty range, which provides an incomplete picture of the sensitivity of the best-fitting result to parameter variations (e.g. Saltelli & Annoni 2010). An uncertainty assessment is important to distinguish relevant processes from less relevant or irrelevant parameters, and to identify the potential relationship between independently estimated parameters.

One class of methods aimed at constraining the uncertainties of the solution is Bayesian inference. It combines prior knowledge with information from observations stochastically. The solution is given in the form of a posterior probability density function (pdf), which naturally expresses model parameter uncertainties. Bayesian methods have been used for a few decades in structural seismology (e.g. Tarantola 1984; Sambridge & Mosegaard 2002; Resovsky & Trampert 2003) and earthquake seismology for finite-fault models (e.g. Fukuda & Johnson 2008; Fukuda *et al.*2009; Minson *et al.*2013, 2014; Jolivet *et al.*2015; Duputel *et al.*2015; Benavente *et al.*2019). In recent years Bayesian methods have become increasingly popular in geodynamic inverse problems as well. For example, Baumann *et al.* (2014); Baumann & Kaus (2015) estimated the rheology of the lithosphere using a Bayesian inverse approach. Moreover, probabilistic estimates of the interseismic coupling pattern were compiled for the central San Andreas Fault (Jolivet *et al.*2015), the Main Himalayan Thrust (Dal Zilio *et al.*2020), Lesser Antilles Arc (van Rijsingen *et al.*2021) and South America subduction zone (Herman & Govers 2020). Fukuda & Johnson (2021) performed a Bayesian inversion for the stress-driven viscoelastic relaxation and afterslip model to estimate the coseismic slip distribution, constant fault frictional parameters and mantle viscosity. Bayesian methods essentially constrain the values and uncertainties of static parameters.

Many data assimilation techniques can be seen as a subclass of Bayesian inference methods. Data assimilation techniques were originally developed within meteorology and oceanography for estimating and forecasting evolving ('dynamic') states of physical systems (Talagrand 1997). The state vector in data assimilation, that is the vector containing the quantities to be estimated, can include the model prediction (or model state), model parameters, model errors, and controls (forcing; Evensen *et al.*2022). The elements of the state vector can consequently be dynamic (e.g. model states) or static (e.g. parameters, so they do not change in time). Data assimilation can combine noisy and spatially and temporally sparse data with imperfect dynamic models. Most data assimilation methods use Bayesian approaches to estimate the state vector. The state vector typically contains the solution variables describing the initial condition of a dynamical system and their temporal evolution. Data assimilation has also been applied for estimating parameters. Parameter estimation is especially common in petroleum engineering, where the properties of subsurface reservoirs are poorly known (e.g. Oliver *et al.*2008). In addition to these applications, data assimilation has also been used in other fields of earth science and engineering. For example, Bunge *et al.* (2003), Nolet (2008) and Fichtner (2011) used data assimilation to constrain the mantle structure from seismological observations. Transient fault slips have been reconstructed from GNSS time-series using data assimilation (Fukuda *et al.*2004, 2008). Kano *et al.* (2013, 2015, 2020) used data assimilation to estimate frictional parameters and states that control slip behaviour at a fault. van Dinther *et al.* (2019), Hirahara & Nishikiori (2019) and Banerjee *et al.* (2023) assimilate near-surface observations into earthquake sequence models to estimate and forecast fault stresses and slip velocities. Our focus will be on data assimilation of geodetic observations in the interseismic phase of an earthquake cycle to estimate elastic parameters and flexural forces related to the overriding plate.

Our understanding of the mechanics of deformation of the megathrust earthquake cycle (interseismic strain accumulation, coseismic rupture and post-seismic relaxation) has greatly improved as continuous geodetic networks became available over the last decades (e.g. Wang *et al.*2012; Avouac 2015; Govers *et al.*2018). Recently, earthquake precursors (Mavrommatis *et al.*2014; Yokota & Koketsu 2015; Socquet *et al.*2017) and permanent deformation (Wesson *et al.*2015) have been considered as part of the seismic cycle. Drivers for horizontal continental movements are understood relatively well (e.g. Diao *et al.*2013; Sun *et al.*2014; Sun & Wang 2015), whereas vertical motions remain difficult to interpret and predict (e.g. Hu *et al.*2014, 2016; Klein *et al.*2016; Freed *et al.*2017). This is furthermore complicated by the fact that vertical motions are more difficult to observe accurately than horizontal motions. However, the sensitivity of vertical motion in the simulation to other aspects of earth process details and rheology hold the potential to more completely resolve the causes of observed surface deformation.

Here we explore the use of data assimilation to estimate model parameters, quantify their probabilistic uncertainties and identify parameter trade-offs. In this first study, we estimate physical quantities that are assumed to be static, that is parameters. We apply the particle method, a Monte Carlo sampling-based Bayesian method, to assimilate (synthetic) interseismic vertical surface displacements sequentially using a mechanical model. This model is intentionally incomplete, simple and numerically efficient, so that we can focus on the performance of the particle method in our context. We also investigate how synthetic marine geodetic data help to further constrain model parameters. We seek to identify the origin of the difference between the spatially variable observations and the mechanical model predictions. These differences can be due to errors in model parameters, processes that are not captured by the mechanical model, representation errors or instrumentation errors. To evaluate the particle method's potential for real scientific challenges we apply the method to real observations prior to the 2011 Tohoku-Oki earthquake. From our results we conclude that data assimilation is very useful for our study region and therefore the method can be applied to other subduction zones.

We begin by providing a brief introduction to sequential data assimilation (Section 2.1), followed by the basics of the sequential importance resampling (SIR) particle filter (Section 2.2). We identify that derived vertical interseismic velocities prior to the 2011 Tohoku-Oki earthquake (Section 3.1) can be explained by flexure of the overriding plate, which we describe using a 2-D conceptual model (Section 3.2). We apply a data-driven approach based on physics to estimate the observational error; a key component in our data assimilation (Section 3.3). Following the synthetic tests (Sections 3.4 to 4.2.2), we conduct tests with real observations prior to the 2011 Tohoku-Oki earthquake (Section 4.3). We then discuss several key aspects related to the importance of seafloor data, model and representation errors, and the feasibility of implementing the particle method in more complex tectonic models (Section 5).

2 DATA ASSIMILATION AND THE PARTICLE METHOD

2.1 A short introduction to sequential data assimilation

Data assimilation aims to estimate the probability of a state vector, given the available sparse and noisy observations. Generally, this state vector $\mathbf{z}$ may contain states, parameters, model errors, and controls. In this study, we focus on sequential data assimilation, and we apply Bayes' theorem to condition the state vector to the observations. Prior estimates of dynamical models, including their parameters, and the likelihood of observations are combined to obtain posterior estimates of the parameters and the corresponding state evolution representing the physical process. In addition to

estimates of the parameters and the state evolution, the probabilistic framework provides estimates of their uncertainties.

To estimate the updated state vector of the physical system, sequential data assimilation generally follows two steps at each time step number t: the forecast (also termed 'propagation') step and the analysis (also termed 'update') step and form one assimilation step. In the forecast step, the estimate at time step $t-1$ (termed 'prior distribution') is propagated forward in time by the physical model to time step t. In the analysis step, the estimate is updated using the new observations.

In solid Earth Sciences, physical processes are not completely understood. The mathematical description of a physical system might (purposely) lack some key physics and therefore the physical model is inherently imperfect. We therefore introduce a model error $\boldsymbol{\eta}_t$ to represent any unresolved processes not taken into account by the model, inaccurate boundary conditions, and discretization errors. With this, the state vector $\mathbf{z}^a_{t-1}$ at time step $t-1$ is evolved to a forecast $\mathbf{z}^f_t$:

$$\mathbf{z}^f_t = \mathcal{M}(\mathbf{z}^a_{t-1}) + \boldsymbol{\eta}_t, \tag{1}$$

where superscripts f and a refer to the forecast and analysis, respectively, and $\mathcal{M}$ represents the model that incorporates our understanding of the physical system (which can be non-linear). Here, we define the state vector $\mathbf{z}$ to contain states $\mathbf{x}$ and model parameters $\boldsymbol{\Theta}$ (i.e. $\mathbf{z} = [\mathbf{x}, \boldsymbol{\Theta}]^\intercal$). Defining the model error is a challenge. Often, the model error is treated as a stochastic additive term (e.g. Carrassi *et al.*2018) or is assumed zero in perfect model tests (e.g. van Dinther *et al.*2019). The model error can also be included in the state vector in some cases (e.g. Evensen 2019) or ascribed to the observation error (e.g. Koohkan & Bocquet 2012) as is done in this study (described below). The prior distribution of model states at time step $t = 0$ needs to be chosen by the user; either based on expert- or historical knowledge of the system. However, the choice of the prior distribution at time step $t = 0$ likely affects the results even after many assimilation steps (Wikle & Berliner 2007).

When observations are available for time step t, the forecast is adjusted by the analysis step. Subsequently, the posterior pdf obtained from the analysis step is used to propagate the model forward and obtain the prior pdf of the next assimilation step (i.e. the forecast). The analysis $\mathbf{z}^a_t$ is conditioned by the available observations $\boldsymbol{d}_t$ at time step t using Bayes' theorem

$$p_m(\mathbf{z}^a_t|\boldsymbol{d}_{1:t}) = \underbrace{\frac{\overbrace{p_d(\boldsymbol{d}_t|\mathbf{z}^f_t)}^{\text{likelihood}}\overbrace{p_m(\mathbf{z}^f_t|\boldsymbol{d}_{1:t-1})}^{\text{prior}}}{\int p_d(\boldsymbol{d}_t|\mathbf{z}^f_t)p_m(\mathbf{z}^f_t|\boldsymbol{d}_{1:t-1})\mathrm{d}\mathbf{z}^f_t}}_{\text{normalization constant: } \frac{1}{c}} = c p_d(\boldsymbol{d}_t|\mathbf{z}^f_t)p_m(\mathbf{z}^f_t|\boldsymbol{d}_{1:t-1}), \tag{2}$$

where subscripts d and m denote the data and model, $\mathbf{z}_t$ denotes the unknown values of the state vector. $\boldsymbol{d}_{1:t} = \{\boldsymbol{d}_1, \boldsymbol{d}_2, \ldots, \boldsymbol{d}_t\}$ and $\boldsymbol{d}_{1:t-1} = \{\boldsymbol{d}_1, \boldsymbol{d}_2, \ldots, \boldsymbol{d}_{t-1}\}$ are the set of observations up to the present time t and past time $t-1$, respectively. $p_m(\mathbf{z}^a_t|\boldsymbol{d}_{1:t})$ is the posterior pdf given the observations $\boldsymbol{d}_{1:t}$ and represents the analysis. $p_m(\mathbf{z}^f_t|\boldsymbol{d}_{1:t-1})$ is the prior pdf, $p_d(\boldsymbol{d}_t|\mathbf{z}^f_t)$ is the likelihood function of the observations at time step t given the state vector at time step t. The result of the data assimilation, the posterior distribution $p_m(\mathbf{z}^a_t|\boldsymbol{d}_{1:t})$, is written as a marginal distribution which is computed recursively for sequential approaches.

In non-Gaussian and non-linear systems, an analytical solution for the posterior pdf is not always possible. Instead, probabilistic sampling with Monte Carlo methods can provide an estimate of the posterior pdf. It is assumed that the state follows a first-order Markov process: the prediction at time t only depends on the state at time $t-1$ (e.g. Evensen *et al.*2022). We can then use Bayes' theorem and calculate the posterior probability as being proportional to the product of the likelihood and the prior pdf (last term in eq. 2).

We can relate the observations at time step t ($\boldsymbol{d}_t$) and the 'true' state vector through:

$$\boldsymbol{d}_t = \mathcal{H}(\tilde{\mathbf{z}}^f_t) + \boldsymbol{\varepsilon}_t, \tag{3}$$

where the observation-operator $\mathcal{H}$ maps the 'true' state vector $\tilde{\mathbf{z}}^f_t$ to the observation space, and the vector $\boldsymbol{\varepsilon}_t$ contains the observation errors with standard deviation σ_t. Observation errors consist of instrumentation- and representation errors (Janjić *et al.*2017). Representation errors arise from unresolved scales and processes, from the observation-operator $\mathcal{H}$ and pre-processing or quality control of observations. Even though unresolved scales and processes are actually captured by the model error (η_t), they are frequently ascribed to the observation error (e.g. Koohkan & Bocquet 2012). Often, the representation error is based on expert knowledge, which is the same for each observation (in space and time).

Sequential Monte Carlo-based methods for non-linear problems include methods such as the Ensemble Kalman Filter (EnKF; Evensen 1994) and the particle filter (PF; van Leeuwen 2009). Monte Carlo-based methods represent the prior probability distribution $p_m(\mathbf{z}^f_t|\boldsymbol{d}_{1:t-1})$ with a finite number of random samples or 'ensemble members' or 'particles'. A PF-based method has been implemented to estimate the fault slip evolution from GNSS time-series (Fukuda *et al.*2004, 2008). The EnKF has recently gained attention in solid-earth dynamics for the estimation of processes such as fault stress and slip evolution (Hirahara & Nishikiori 2019; van Dinther *et al.*2019). The EnKF assumes Gaussian error statistics and applies partial linearization of the observation prediction to reduce computational costs. For a comparison of different assimilation methods, we refer the reader to Evensen *et al.* (2022). In this study, we use a numerical model that is computationally fast, which allows us to run a large number of simulations to sample the prior distribution and apply the PF (or particle method) to sample the prior distribution. When the number of particles is limited, the PF may suffer from particle or ensemble degeneracy (see Section 2.2; Snyder *et al.*2008). In such a case, the use of other methods may be preferred.

2.2 The particle method

In this study we explore the applicability of the particle method. The key idea of the particle method is to use a Monte Carlo approach to represent an arbitrary probability density function as a number of discrete weighted samples. Each particle contains one set of values of the state vector elements. A selected data set is fed to the particle method algorithm, which sequentially assimilates data into the model using a number of time steps (which can also be a single step) and produces posterior distributions of the state vector (Fig. 1a). We use the sequential importance resampling (SIR) PF in our analysis (e.g. van Leeuwen 2009; Fig. 1b). The basic steps of the SIR PF for a single assimilation window include propagation (i.e. the forecast step), importance weighting (i.e. the analysis step), resampling and jittering (Fig. 1b). The details of the SIR PF are explained in detail below.

The SIR PF starts with initializing the state vectors for all particles $\{\mathbf{z}^i_{t=0}\}_{i=1,\ldots,N_e}$, with N_e being the number of particles. The initial particles represent the prior probability distribution at $t = 0$. The

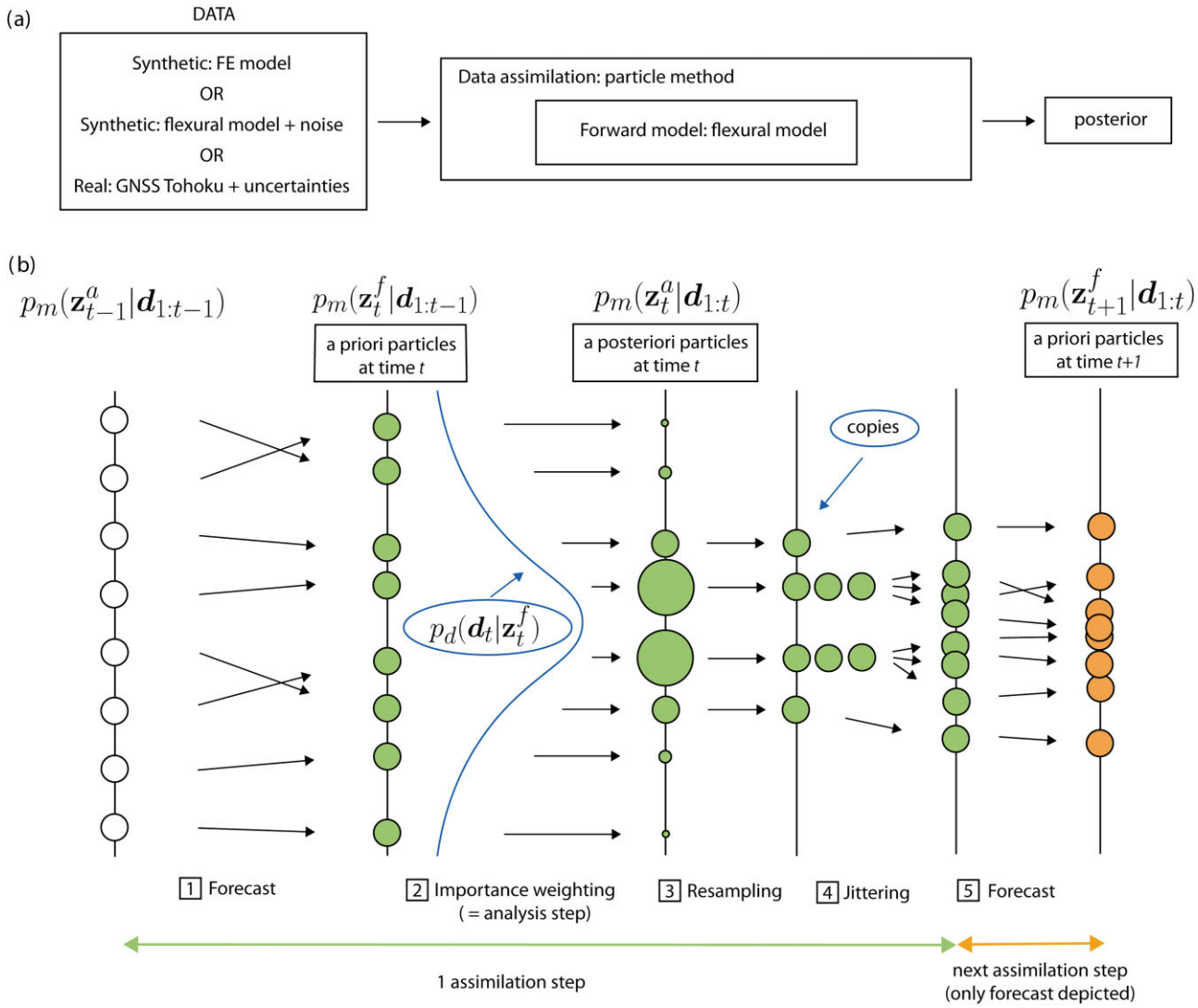

Figure 1. (a) Overview of how data assimilation is related to the (synthetic) data, forward model and posterior distribution. In our synthetic tests, data is either sampled from the finite element model (FEM) or the same forward model used in data assimilation. In real-data experiments we use interseismic velocities derived from GNSS prior to the Tohoku-Oki earthquake. Data are assimilated using the particle method into the forward model to obtain posterior estimates of the state vector. (b) Schematic of the sequential importance resampling particle filter. Crossing of the black lines in step 1 corresponds the case where a state is propagated forward in time and thus a different state is obtained. The blue curve is the observation likelihood function $p_d(\boldsymbol{d}_t|\mathbf{z}^f_t)$. The size of the circles denotes the weight of the particles. White, green and orange colours of the circles denote the time steps $t-1$, t and $t+1$, respectively.

initialization is based on prior knowledge of the model parameters or initial conditions. Subsequently, each particle is propagated forward in time (from $t-1$ to t, eq. 1) to obtain the prior probability distribution at time step t, $p_m(\mathbf{z}^f_t|\boldsymbol{d}_{1:t-1})$ (Fig. 1b step 1). In our parameter-estimation problem, we purposely let parameters vary with time, but assume that parameters do not vary as much as states and that parameters will converge over time. For the first time step, we thus propagate from $\mathbf{z}_{t=0} = [\mathbf{x}_{t=0}, \boldsymbol{\Theta}_{t=0}]^\intercal$ to $\mathbf{z}^f_{t=1} = [\mathbf{x}^f_{t=1}, \boldsymbol{\Theta}^f_{t=1}]^\intercal$. The forward model in our problem requires parameters from the previous time step as input and only propagates the states to the next time step such that $\boldsymbol{\Theta}^f_{t=1} := \boldsymbol{\Theta}_{t=0}$. The operator $\mathcal{M}$ thus does not affect the value of the parameters. As a consequence, we only need to initialize parameters at $t=0$. Then, each particle is weighted by its fit to the observations $\boldsymbol{d}_t$ at time step t to obtain particles that represent the posterior probability distribution at time step t, $p_m(\mathbf{z}^a_t|\boldsymbol{d}_{1:t})$ (Fig. 1b step 2), which is represented by a weighted sum of Dirac-delta functions (van Leeuwen 2009):

$$p_m(\mathbf{z}^a_t|\boldsymbol{d}_{1:t}) = \sum_{i=1}^{N_e} w^i \delta\left(\mathbf{z}^f_t - \left(\mathbf{z}^f_t\right)^i\right), \tag{4}$$

where for each particle i the importance- or particle weight w^i_t at time step t is computed with

$$w^i_t = \frac{p_d\left(\boldsymbol{d}_t|\left(\mathbf{z}^f_t\right)^i\right)}{\sum_{j=1}^{N_e} p_d\left(\boldsymbol{d}_t|\left(\mathbf{z}^f_t\right)^j\right)}. \tag{5}$$

Particles with a better fit to the observations obtain a relatively higher weight. For our parameter-estimation problem, the analysis is only applied on the parameters $\boldsymbol{\Theta}^f_t$.

The user of the SIR PF can choose a function to represent the probability density of the observations, $p_d(\boldsymbol{d}|\mathbf{z}^f)$. Typically, this

function is assumed to be Gaussian, but we use a Lorentz density in our analysis. The shape of the Lorentz density is very similar to a Gaussian density, but provides broader tails. Broader tails ensure that fewer particles have a negligible weight, such that they can be considered in the analysis. The likelihood at time step t for observation d_t is given by the Lorentz density:

$$p_d(d_t|\mathbf{z}_t^f) = \frac{1}{1 + \frac{[d_t - \mathcal{H}(\mathbf{z}_t^f)]^2}{\sigma_t^2}}, \tag{6}$$

in which $\mathcal{H}$ is the observation-operator and σ_t is the standard deviation of the observation error. In our problem, the dynamic model equations directly translate the model parameters into model outputs in the observation space. Thus, the part of $\mathcal{H}$ that relates to the states performs a direct mapping of the states to the observation space. The parameters in the state vector are not being observed and therefore disregarded by the observation-operator $\mathcal{H}$ (see eq. 16).

One of the potential drawbacks of the PF can be that only a few particles have a large weight and the remaining particles have near-zero weight (e.g. van Leeuwen 2009). This phenomenon is called particle degeneracy (or ensemble degeneracy, see Index and Synonyms). This means that the particles do not represent the desired probability function of the model parameters anymore and the performance of the PF deteriorates. The statistical information of the estimation thus becomes insubstantial. With a Lorentz density described above it is less probable to have particle degeneracy (van Leeuwen 2003; Vossepoel & van Leeuwen 2007). Resampling is a measure in the SIR filtering process to avoid degeneracy of importance weights. There are many resampling techniques available, as reviewed by Douc & Cappe (2005). We use residual resampling, which distinguishes itself by reducing the variance due to sampling (Lui & Chen 1998). Particles with high weight are duplicated and particles with low weight are not copied, while the number of particles, N_e, remains constant (Fig. 1b step 3, see Supplementary Text S1 for details). Resampling generates equally weighted particles representing the posterior probability distribution at time t, $p_m(\mathbf{z}_t^a|\boldsymbol{d}_{1:t})$ (Fig. 1b step 3).

Resampling aims to reduce the diversity of particles (i.e. fewer unique state values) to decrease the ensemble variance, but the reduction can be too large. Another disadvantage of resampling is that it requires costly interprocessor communication, as the resampling step requires all weights to be known. Therefore, it is desired to minimise the number of resampling steps. Commonly, resampling only occurs when the variance of the weights is larger than a predefined threshold. A measure of particle degeneracy is the effective sample size (ESS). The ESS is defined as the number of samples required to match the precision if we were randomly sampling from the target distribution (Kong 1992; Kong *et al.*1994):

$$ESS \approx \frac{1}{\sum_{i=1}^{N_e} w_i^2}. \tag{7}$$

A commonly used threshold, N_T, is that resampling occurs if the ESS is smaller than half the number of particles ($N_T = N_e/2$) (Doucet & Johansen 2008), which we will use throughout our experiments.

Resampling may lead to particle degeneracy due to the reduction of the number of distinct particles.

Increasing the number of particles to improve the diversity of the particles is not an ideal solution as it also results in larger computational times. To alleviate this, we apply a small perturbation ('jittering') to the particles after resampling which increases the spread of the particles (Fig. 1b step 4; Gordon *et al.*1993), such that it does not significantly alter the posterior distribution. There is no consensus on how to choose the jitter. Conventionally, jitter is determined by trial and error (as done in Section 4.2.1). In that case, the random perturbation for the jittering is drawn from a normal distribution with zero mean $\sim \mathcal{N}(0, \sigma'^2)$, in which σ' is a number that must be specified by the user. Alternatively, the jitter can be a fraction of the ensemble variance, where the scaling factor C is determined by trial and error (as done in Sections 4.2.2 and 4.3). The random perturbation for the jittering is subsequently drawn from a normal distribution with zero mean $\sim \mathcal{N}(0, C^2\sigma_{\text{ens}}^2)$, in which σ_{ens} is the standard deviation of the ensemble and the scaling factor C must be specified by the user. However, in this study, we sometimes purposely choose relatively large perturbations when new observations are available to help steer the evolution of the parameter estimates, such that the filter can effectively decrease the misfit between model predictions and observations (as done in Section 4.1.2). Note that jittering is generally not needed when models have a stochastic component (often in atmospheric and oceanography studies), in which case the same starting condition can result in different trajectories. Because our models, as most solid earth geophysical models, lead to the same trajectory with the same starting conditions, we choose to apply jittering. The particles obtained after jittering are propagated to the next time step, $p_m(\mathbf{z}_{t+1}^f|\boldsymbol{d}_{1:t})$ (orange colours, Fig. 1b step 5). When applying jittering the posterior distribution at the last time step may may not overlap with the prior distribution initialized at the beginning of the assimilation, which can be useful when there is little or incorrect prior knowledge of the unknown state vector elements.

3 INTERSEISMIC VERTICAL DEFORMATION AT A SUBDUCTION MARGIN

3.1 Geodetic observations

We analyse daily site coordinate solutions (Nakagawa 2009) processed in ITRF2008 (Altamimi *et al.*2011), operated by the Geospatial Information Authority (GSI) of Japan. We extract time-series prior to the 2011 Tohoku-Oki earthquake between January 1997 and May 2000. Just as Loveless & Meade (2010), we end the time-series in mid-2000, due to seismic swarms from June to August 2000 offshore central Japan (Hamada 2000), the 2003 M_w 8.0 Tokachi-Oki earthquake (Yamanaka & Kikuchi 2003), the 2003 M_w 6.8 earthquake off Fukushima (Ozawa *et al.*2012) and the 2005 M_w 7.2 Miyagi earthquake (Okada *et al.*2005). The time-series do include effects from two significant events in March 1997 and May 1998 (Nishimura *et al.*2007; Loveless & Meade 2010), but our parametric model used to fit the position time-series isolates the coseismic signal (described below).

We extract the deformation by means of a least-squares fit to a parametric model, which consists of a linear trend, annual and semi-annual effects and possible offsets due to sudden events (e.g. coseismic deformation and instrument- and antenna changes). The displacement time-series at site i is expressed as:

$$\begin{aligned}\boldsymbol{u}^i(t) = \boldsymbol{a}^i + \boldsymbol{b}^i t + \boldsymbol{c}^i \cos(2\pi t) + \boldsymbol{d}^i \sin(2\pi t) + \boldsymbol{e}^i \cos(4\pi t) \\ + \boldsymbol{f}^i \sin(4\pi t) + \sum_{k=1}^{K} \boldsymbol{g}^i \theta(t_k - t),\end{aligned} \tag{8}$$

where $\boldsymbol{u}$ is the displacement vector composed of east-, north- and vertical components at date t; $\boldsymbol{a}$ is the displacement at time 0; $\boldsymbol{b}$ is the slope representing the interseismic strain accumulation; $\boldsymbol{c} - \boldsymbol{f}$ are annual and semi-annual seasonal coefficients; $\boldsymbol{g}$ is the change in deformation due to a sudden event; θ is the Heaviside function and t_k is the time of a sudden event. Then, we reference all displacements relative to the GNSS station FUKUE (station ID: 950462, 128.8°E, 32.7°N) as we regard this reference station as being on the stable Amurian Plate. As part of our data processing, we find estimates for the unknown coefficient vectors $\boldsymbol{a}$, $\boldsymbol{b}$, $\boldsymbol{c}$, $\boldsymbol{d}$, $\boldsymbol{e}$, $\boldsymbol{f}$ and $\boldsymbol{g}$ for each GNSS time-series. Note that in our data assimilation, we assimilate daily vertical displacements $\boldsymbol{u}^i(t)$-$\boldsymbol{u}^{\mathrm{FUKUE}}(t)$ and use these coefficient vectors to address processes that we do not model (see Section 3.3).

A transect coinciding with the centre of the pre-seismic locked region in Loveless & Meade (2010) is defined (solid black line in Fig. 2a). Geodetic observations are selected within 30 km (i.e. the half swath width) both north and south of the transect to create a 2-D profile of surface displacements (Fig. 2c). Surface displacements show a clear coherent landward motion during the interseismic phase (Figs 2a and b). The eastern side along the transect exhibits subsidence, and the western side exhibits uplift (Fig. 2c).

3.2 Interseismic deformation model and data assimilation implementation

GNSS data in Fig. 2c predominantly show forearc subsidence and uplift of the arc and backarc, suggesting flexure at a large scale. Interseismic deformation of the overriding plate is driven by plate convergence via locking of asperities and flow in the mantle wedge. Interseismic deformation of the overriding plate is largely recovered during megathrust earthquakes (Mazzotti *et al.*2002). Therefore, we hypothesize that the large-scale vertical deformation reflects flexure of an elastic plate. We thus apply an elastic flexure model (Vening Meinesz 1931; Walcott 1970) in the forecast step of our PF.

The 2-D analytical model consists of an elastic overriding plate of thickness H, where buoyancy forces are provided by the asthenospheric mantle with density $\rho_{\mathrm{m}} = 3200\ \mathrm{kg\,m^{-3}}$ (Fig. 3a). At least two basal forces/tractions are needed to generate the observed uplift and subsidence zones (Fig. 2c). In our forward model we apply two vertical line loads on the base of our overriding plate (Fig. 3a). Our data assimilation scheme aims to constrain the elastic plate thickness H, the locations of the line loads y_1 and y_2 and their magnitudes q_1 and q_2.

As we use an elastic flexure model to estimate the vertical deflection of the upper plate, the response to forcings are by definition instantaneous. However, for our data assimilation problem, we need to introduce a temporal component to our parameters and states. The vertical deflection of the upper plate without horizontal forcing satisfies the following fourth-order ordinary differential equation with a temporal component (modified from Turcotte *et al.*1978):

$$D(t)\frac{\mathrm{d}^4 d_y(x,t)}{\mathrm{d}x^4} + (\rho_m - \rho_i)g d_y(x,t) = q(x,t) \tag{9}$$

in which x is the horizontal coordinate, t is time, ρ_{m} is the asthenospheric density, ρ_i is the density above the surface, g is the gravitational acceleration, $d_y(x,t)$ is the deflection of the upper plate, $q(x,t)$ describes the vertical loads, $D(t) = EH^3(t)/(12(1-\nu^2))$ is the flexural rigidity, E is Young's modulus, H is the effective elastic thickness of the lithosphere and ν is Poisson's ratio. Variations in flexural rigidity of the lithosphere are largely determined by H due to its dependency on the cube of H. We therefore fix the elasticity parameters and only solve for H. Our model input parameters are depicted in Table S2. The solution to eq. 9 is given by the following forward model

$$d_y(x,t) = \int_{-\infty}^{\infty} q(y,t)G(x,y,t)\mathrm{d}y \tag{10}$$

$$G(x,y,t) = \frac{\frac{2\pi}{\lambda}\exp\left(-\frac{2\pi}{\lambda}|x-y|\right)}{2g(\rho_m-\rho_i)}\left[\cos\left(\frac{2\pi}{\lambda}|x-y|\right)+\sin\left(\frac{2\pi}{\lambda}|x-y|\right)\right] \tag{11}$$

in which $\lambda(t) \equiv 2\pi/([(\rho_m - \rho_i)g/(4D(t))]^{1/4})$ is the wavelength. $G(x, y, t)$ represents the vertical surface displacement at horizontal coordinate x due to a unit line load acting at horizontal coordinate y. We estimate H from D (and thus λ) and the time-dependency of G derives from the time dependency of λ and y. The Green's function is convolved with a load function $q(x, t)$ (Fig. 3a, eq. 10):

$$q(x,t) = q_1(t)\delta(x - y_1(t)) - q_2(t)\delta(x - y_2(t)) \tag{12}$$

In our data assimilation problem, we also need a mapping from the previous time step to the next time step for the forecast step (eq. 1). For our data assimilation experiments where we assimilate displacement time-series, eq. 10 is adapted as follows to include a mapping from time step $t-1$ to time step t:

$$d_y(x,t) = \int_{-\infty}^{\infty} q(y,t-1)G(x,y,t-1)\mathrm{d}y. \tag{13}$$

Here, we use model parameters $\boldsymbol{\Theta}$ from time step $t-1$ to estimate the displacements d_y (i.e. states $\mathbf{x}$) at time step t. We also conduct time-invariant data assimilation problems, where we assimilate velocities. These data assimilation experiments consist of one assimilation step and parameters do not vary with time (see Supplementary Text S4 for modified data assimilation equations). For this time-invariant problem (see Section 4.1.1), eqs 10 and 12 are modified to exclude the temporal component and allow for an estimation of vertical velocities:

$$v_y(x) = \int_{-\infty}^{\infty} \dot{q}(y)G(x,y)\mathrm{d}y \tag{14}$$

and

$$\dot{q}(x) = \dot{q}_1\delta(x - y_1) - \dot{q}_2\delta(x - y_2), \tag{15}$$

respectively, where v_y is the deflection rate of the upper plate and $\dot{q}$ is the loading rate. Moreover, we also adopt a time-invariant plate thickness H, which can be derived from the wavelength (eq. 11).

Depending on the data assimilation experiment (Section 3.4), the vector $\boldsymbol{\Theta}$ consists of a combination of the parameters H, y_1, y_2, $\dot{y}_1$, $\dot{y}_2$, $\dot{q}_1$ or $\dot{q}_2$, listed in the third column of Table 1. The state $\mathbf{x}$ contains either the predicted displacements d_y or velocities v_y at all the GNSS station locations. In the forecast step, eq. 13 is used to propagate the state $\mathbf{x}$ from time step $t-1$ to t in the time-variant problem. For the time-invariant problem, eq. 14 is used to estimate the forecast state from the initial guess. The model error $\boldsymbol{\eta}$ is assumed zero for both the states $\mathbf{x}$ and model parameters $\boldsymbol{\Theta}$. Our models directly translate the parameters into predicted displacements or velocities at the same locations as the actual observations. The model equations do not affect the parameter values. Thus, in our problem we set the parameter values of the next time step to that of the previous time step after resampling (and jittering). Therefore, the part of $\mathcal{H}$ that relates to the states performs a direct mapping of the states to the observation space and the parameters are disregarded. The observation-operator $\mathcal{H}$ is approximated by the linear observation-operator H:

$$H = \begin{bmatrix} I_{S\mathrm{x}S} & O_{S\mathrm{x}P} \\ O_{P\mathrm{x}S} & O_{P\mathrm{x}P} \end{bmatrix}, \tag{16}$$

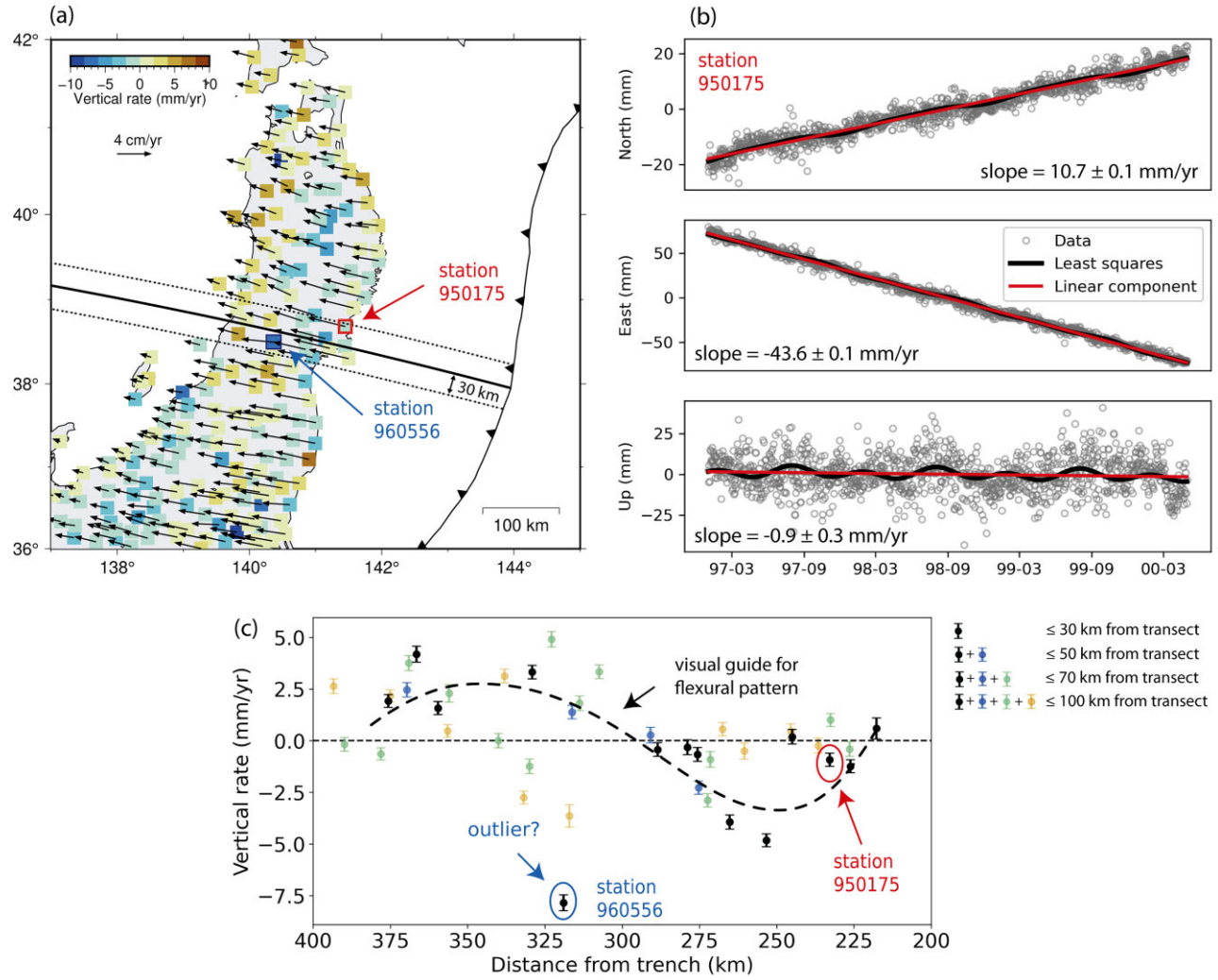

Figure 2. (a) Vertical and horizontal velocities in Northeastern Japan between January 1997 and May 2000. Displacements are referenced to GNSS station FUKUE (station ID: 950462, 128.8°E, 32.7°N). The selected transect (solid black line) coincides with the largest pre-seismic coupling fraction perpendicular to the trench following Loveless & Meade (2010). The dotted lines show the upper and lower bounds of the swath profile; 30 km north and south of the solid line. Black vectors indicate the horizontal GNSS velocities, whereas coloured squares denote the magnitude of the vertical velocities. (b) Time-series of the north-, east- and vertical surface displacements for station 950175 denoted by the red outlined square is shown in panel (a). (c) Vertical rate as a function of distance from trench along swath profiles with half width 30, 50, 70 and 100 km. We select data from a 30 km half width swath as data within a larger swath deviate from the flexural pattern. Error bars correspond to uncertainty bands of the linear trend.

where S is the number of states and P is the number of parameters in the state vector.

3.3 Quantitative constraints on errors in real data and model

The length of the data time-series allows us to estimate the linear trend with a small uncertainty. For example, the uncertainty in the velocity (in **b** in eq. 8) for station 950175 is 0.3 mm yr^{-1} in the vertical direction (Fig. 2b). However, the differences between the least squares fit and the data remain relatively large (i.e. the differences between grey dots and black line, Fig. 2b). These differences are due to noise in the data and processes not considered in the parametrization. Moreover, there are possibly other linear processes present in the data that are not related to flexure. Our flexural model aims to reproduce the linear trend. It is clear that the velocities derived from the data in Fig. 2c (i.e. the black error bars) cannot be fitted well by a simple flexural model like the visual guide. The uncertainty in the velocity is not representative of the discrepancies between our modelled observations and real geodetic observations, which are attributed to instrumentation and representation errors. Representation errors are generally based on expert knowledge and do not vary in space and time. For our synthetic data experiments we draw the observation error from a random distribution and are thus more or less constant in space and time (except for Experiment 5, Sections 3.4 and 4.2.2). Because the discrepancies between our model forecast and the actual data are relatively large (Fig. 2c), we need to properly address the representation error to vary both temporally and spatially, which is explained further below.

The data times-series contain signals from various processes. We can isolate some of these processes (i.e. linear trend, annual and semi-annual components and steps) from a parametrization of the data time-series, as explained in Section 3.1. Next to these

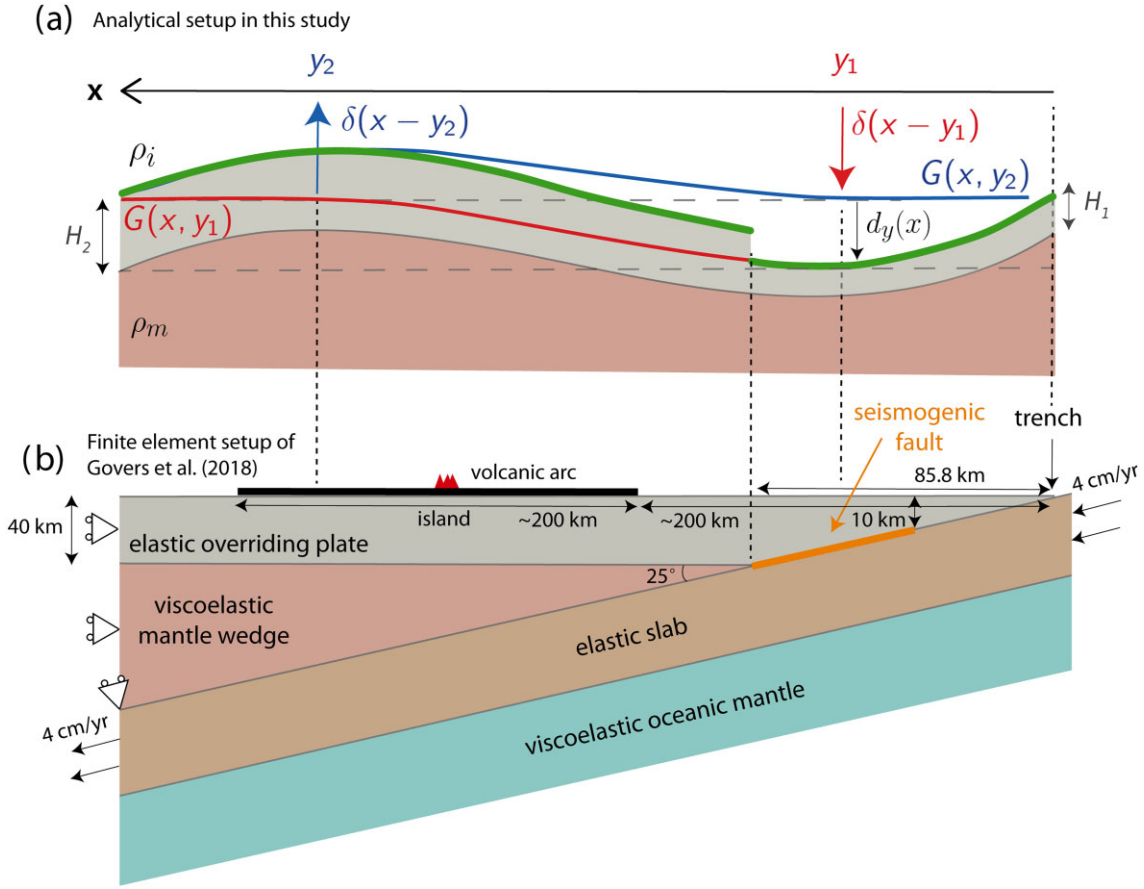

Figure 3. (a) Forward model setup depicting elastic flexure. The two line loads $\delta(x-y_1)$ and $\delta(x-y_2)$ at y_1 and y_2, respectively, act on an infinite elastic plate with thicknesses H_1 and H_2. The elastic plate is underlain by an asthenospheric mantle, resulting in a hydrostatic restoring force $\rho_m g d_y$ and driving surface force $\rho_i g d_y$. The green line is the integrated result of the responses by the two line loads. (b) Geometry of the finite element model from Govers *et al.* (2018) used to generate synthetic data for Experiments 1–3 (Table 1). H_1 and H_2 are the plate thickness right and left of where the taper in thickness of the upper plate ends in the finite element model (b), respectively.

Table 1. Overview of data assimilation experiments. Our forward models either assimilate time-invariant surface velocities or time-variant surface displacements.

Experiment number	Velocity/displacement outputs	Parameters	Data	Figures and Tables
1	Velocity	$H, y_1, y_2, \dot{q}_1, \dot{q}_2$	FE model	Figs 4–6, Table 2
2	Velocity	$H_1, H_2, y_1, y_2, \dot{q}_1, \dot{q}_2$	FE model	Fig. 4, Table 2
3	Displacement	$H, y_1, y_2, \dot{q}_1$	FE model	Figs 7, 8, Table 3
4	Displacement	$\{dH_k\}_{k=1,\ldots,16}$	Synthetic (identical twin)	Fig. 9
5	Displacement	$H, y_1, y_2, \dot{q}_1$	Synthetic (identical twin) with realistic representation errors	Figs 10, 11
6	Displacement	$H, y_1, y_2, \dot{q}_1$	Tohoku interseismic velocities	Figs 12, 13

Note: H is the uniform elastic thickness of the overriding plate, y_1 and y_2 are the locations of the two line loads, $\dot{q}_1$ and $\dot{q}_2$ are the magnitudes of the two line load rates. dH is the deviation from a uniform plate thickness H.

processes, the data time-series may also contain spatially correlated errors. To analyse these spatially correlated errors, we first retrieve the GNSS residual time-series x_{ij} by subtracting the least squares fit from the observation time-series, with $i = 1, \ldots, n$ time steps at $j = 1, \ldots, p$ locations. The GNSS residual time-series are highly correlated as shown by a mean Pearson correlation coefficient of 0.7 (Fig. S2). The strong spatial correlation among the residual time-series may be caused by the sum of various systematic errors, which are commonly referred to as the common-mode error (CME; Dong *et al.*2006; Kumar *et al.*2020). Even though we do not fully understand the nature of these systematic errors, we can isolate them given their spatial correlation. We seek to identify the common-mode error to properly address the systematic errors in our data assimilation simulations.

We perform an empirical orthogonal function (EOF) analysis (Preisendorfer 1988) to reveal the internal structure of our data, which we use to identify (1) a bias (the common-mode error) in the GNSS network explaining a large portion of the variance in the data

and (2) a noise term that we identify as the instrumentation error (see Supplementary Text S2). The structures found in the spatial dimension are the EOFs and temporal structures are the principal components (PCs). The first mode contributes most to the variance, the second mode explains most of the remaining variance, and so on. We define the first mode as the systematic common-mode error. We assume that the remaining modes are due to noise from instrumental uncertainties.

We assume that the total observation error is the sum of errors from the linear trend, annual- and semi-annual components, steps, common-mode- and instrumentation errors in our real-data assimilation experiments. The variance of the total observation error for the real observations as a function of time ($\boldsymbol{\sigma}_t^2$ in eq. 6) is then given by:

$$\boldsymbol{\sigma}_t^2 = \overbrace{\underbrace{\boldsymbol{\sigma}_{t,\text{linear}}^2 + \boldsymbol{\sigma}_{t,\text{season}}^2 + \boldsymbol{\sigma}_{t,\text{step}}^2}_{\text{parameterisation}} + \boldsymbol{\sigma}_{t,\text{CME}}^2}^{\text{representation}} + \overbrace{\boldsymbol{\sigma}_{t,\text{noise}}^2}^{\text{EOF}} \tag{17}$$

in which $\boldsymbol{\sigma}_{t,\text{linear}}$ is the standard deviation (SD) of errors due to the uncertainty in the linear trend, $\boldsymbol{\sigma}_{t,\text{season}}$ is the SD of errors due to seasonal effects, $\boldsymbol{\sigma}_{t,\text{step}}$ is the SD of errors due to abrupt changes in the time-series (e.g. coseismic signals), $\boldsymbol{\sigma}_{t,\text{CME}}$ is the SD of errors corresponding to a common-mode error, and $\boldsymbol{\sigma}_{t,\text{noise}}$ is the SD of instrumentation errors. Results show that the common-mode error is the largest component of our total estimated representation error (e.g. approximately 76 per cent for station 940032, Fig. S3).

3.4 Setup of data assimilation experiments

We perform three types of data assimilation experiments, two types of experiments with synthetic observations (identical and non-identical experiments) and a third type with real observations. All data assimilation experiments use the simple flexural model described in Section 3.2 and Fig. 3a. A non-identical twin experiment involves synthetic data sampled from a different geophysical model than the model that we use to assimilate the data, specifically the finite element (FE) model of Govers *et al.* (2018) (Fig. 3b, explained in Section 4.1.1). Model parameters (i.e. the 'truth') of the FE model are known, facilitating a direct comparison with parameters estimated from data assimilation. In an identical twin experiment, synthetic data is generated with the same geophysical model as used in the data assimilation (Fig. 3a), hence the 'truth' is known also. Gaussian noise is added to the synthetic data. The mean of the Gaussian prior at the beginning of the data assimilation that is specified by the user, should be different than the true model parameter.

In all data assimilation experiments we define the state vector $\mathbf{z}$ as a set of model states and parameters used to describe the system through model equations. The set of parameters for each experiment is shown in Table 1. The selected prior distributions are shown in Table S1 and choices regarding the total observational error, jittering and number of particles are explained in Supplementary Text S3. In this research we do not include model errors in the state vector. However, an assumption of a zero model error in eq. 1 may not be valid for our real-data experiments. Discrepancies between observations and the predicted observations will consequently be mapped into representation errors (Section 3.3). Representation errors are defined as errors that occur as a result of the model not being representative for the actual physics. Note that instrumentation errors are simultaneously estimated with representation errors (Section 3.3). The PF uses a likelihood that is based on the combined instrumentation and representation error. Thus, the standard deviation of the total observational error (instrumentation + representation) is the σ_t value in eq. 6.

4 RESULTS AND ANALYSIS

4.1 Non-identical twin experiments

4.1.1 Assimilation of time-independent synthetic data (Experiments 1 and 2)

Data assimilation Experiments 1 and 2 are non-identical twin experiments. Here, we use constant velocities to estimate model parameters. We use eqs 11, 14 and 15 to describe the system and assimilate velocities and do not let parameters vary over time. As the problem is now time-invariant, the data assimilation equations need to be slightly modified to be time-independent (see Supplementary Text S4). These experiments exist of a single assimilation step without resampling or jittering.

The synthetic data are sampled from the reference model of Govers *et al.* (2018) (Fig. 3b). Their FE model is build using the code GTECTON (Melosh & Raefsky 1983; Govers & Wortel 1993), which solves the momentum equation for plane strain. The FE model consists of an elastic overriding plate and slab, and a viscoelastic mantle wedge and oceanic mantle with a Maxwell viscoelastic rheology (see Fig. 3b). The FE model predicts the surface displacements throughout the earthquake cycle, where the duration of one earthquake cycle is 200 yr and the relaxation time (τ) is 8 yr. The thickness of the overriding plate is taken to represent the true thickness in our flexure model. The true location and magnitude of the line loads are unknown. We only sample from the model output of steadily evolving vertical surface displacements corresponding to the interseismic phase, between 15τ and 24τ after the last earthquake. We purposely do not superimpose noise on samples from the model output. Although this is inconsistent with the assumptions in the data-assimilation formulation, this allows us to determine if our conceptual model can reproduce results for similar model parameters as the FE model, without noisy data potentially affecting the results. We do ascribe a standard deviation of the observational errors of 1 mm yr^{-1} to Experiments 1–2 to allow for small differences between our model and the FE model (this is the σ value in eq. 6).

We first sample synthetic velocity observations from the FE model at ∼15 km intervals in both continental and marine domains. In Japan, this is currently a realistic interval for the onshore GNSS network. In Experiment 1, vertical velocities are assimilated with a model with a uniform plate (Table 1). This yields a plate thickness of 37.3 ± 2.0 km (Table 2), which is slightly smaller than the truth of 40 km. Experiment 2 is based on the recognition that the overriding plate thickness linearly decreases towards zero at the trench (Fig. 3b). We therefore estimate two thicknesses in Experiment 2, thickness H_1 between the trench and the coast (∼86 km from the trench) and thickness H_2 for the land part of the model. The results show no significant difference between the estimated H_2 and the truth (Table 2). However, H_1 differs substantially from the average value of the truth in that it is approximately 1 per cent thicker than H_2. This can be explained by the fact that isostatic support by the slab in the FE model reduces the vertical surface velocity, which results in a stiffer, thicker plate estimate from the data assimilation. Relative to Experiment 1, standard deviations of the thickness estimates are larger because fewer observations are available per parameter to constrain it. The two line loads are estimated to be located at approximately 35 and 325 km from the trench (Table 2).

Table 2. Estimated model parameters and their standard deviations from Experiments 1–2. The true parameters correspond to the parameters used in the reference model of Govers *et al.* (2018). See text for symbol definitions.

Model	Experiment number	H_1 (km)	H_2 (km)	y_1 (km)	y_2 (km)	$\dot{q}_1$ (Pa m^{-1} s^{-1})	$\dot{q}_2$ (Pa m^{-1} s^{-1})
Truth							
FE	–	Taper from 40.0 to 0.0	40.0	—	—	—	—
Regularly distributed synthetic data in continent and ocean							
Uniform	1	37.3 ± 2.0	37.3 ± 2.0	35.6 ± 1.7	326.5 ± 4.7	2065 ± 16	711 ± 16
Two plates	2	38.1 ± 4.6	37.7 ± 4.6	35.6 ± 2.8	325.2 ± 6.6	2068 ± 20	716 ± 15
Synthetic continental data only							
Uniform	1	39.6 ± 2.8	39.6 ± 2.8	27.1 ± 4.4	325.0 ± 4.9	2060 ± 16	717 ± 16
Synthetic continental and near trench data							
Uniform	1	37.6 ± 2.0	37.6 ± 2.0	34.7 ± 2.5	324.8 ± 4.3	2064 ± 16	707 ± 15
Two plates	2	38.8 ± 4.8	37.3 ± 4.5	34.4 ± 3.5	323.7 ± 6.8	2062 ± 20	712 ± 15

Next, we investigate the sensitivity of the parameter estimation to network aperture. We apply data assimilation to both the uniform and two-plate model, to test if any of the model parameters are sensitive to the choice of the data distribution. The results of a uniform plate experiment where only continental data are assimilated show that most parameter estimates are similar, except for the line load location y_1, which is underestimated by more than 20 per cent compared to the case where seafloor data is used (Table 2). The two experiments (uniform plate and two-plate) using continental and near-trench (marine) observations only (see Fig. 4 for locations) intend to mimic the availability of the present GNSS and GNSS/A observations. The resulting parameters estimates are similar to the estimates for complete data coverage, highlighting the relevance of marine geodetic observations near the trench.

Finally, we investigate the ratio between the number of synthetic on- and offshore data and the optimal positioning of the synthetic seafloor stations. We fix the number of onshore data stations to 10 which are spaced approximately every 15 km. The number of synthetic seafloor stations varies between 2 and 15 stations (Fig. 5). We find that the parameters y_2, $\dot{q}_1$, $\dot{q}_2$ are not sensitive to the ratio between the number of synthetic on- and offshore data as long as the synthetic seafloor data are evenly distributed (Fig. 5). Parameters H and y_1 are somewhat sensitive to the ratio between the number of synthetic on- and offshore data, but in all cases (Figs 5a–d) the estimates overlap within one standard deviation. In another test, we keep the same number of onshore stations fixed, include a single synthetic offshore station and vary the position of the single synthetic offshore station. Similarly, we find that the estimates for the parameters y_2, $\dot{q}_1$ and $\dot{q}_2$ are insensitive to the addition of a single offshore observation (Figs 6c–e). For parameter H, all estimates mostly overlap with the estimate obtained with evenly distributed data (Fig. 6a). However, the strongest correspondence is found when the observation is located between 25 and 100 km from the trench. For parameter y_1, the optimal range of the observation location is between 50 and 150 km if we assume that the truth is better described when we include evenly distributed data (Fig. 6b). These results highlight the importance of near-trench data and that the fit does not simply improve with the use of more data. When only continental data is used, the estimate for particularly y_1 deteriorates, if we assume that the truth is better described when we include evenly distributed data, and its uncertainty decreases (Table 2). Subsequently, the range of model outputs near the trench becomes larger. Hence, the predicted model outcomes and parameter estimates improve with the inclusion of near-trench data.

4.1.2 Assimilation of synthetic time-series (Experiment 3)

Experimental setup

For non-identical twin Experiment 3 we include an evolving state and use synthetic surface displacement time-series (i.e. the forward model is time-dependent). We assume a standard deviation of the observation error of 4 mm. Experiment 3 consists of 67 time/assimilation steps and each time step is equivalent to 0.125τ in the FE model. We use eqs 11, 12 and 13 to describe the system to assimilate displacements. The line loads in eq. 12 are time-dependent and are expressed in Pa m^{-1} to produce surface displacement outputs. We assume that $q(y, t)$ varies linearly with time due to interseismic deformation after many data assimilation steps. We estimate the slope of this linear relation, that is $\dot{q}(y, t)$ (Pa m^{-1} s^{-1}) and assume that its estimate converges with time so that $q(y, t)$ varies linearly. Parameters $\dot{q}_1$ and $\dot{q}_2$ control the magnitude of maximum uplift and subsidence. From Experiments 1 and 2 we found that the ratio between $\dot{q}_1$ and $\dot{q}_2$ is around 2.9. We saw that the ratio between the loads tends to be stationary, which suggests that the value of these loads are coupled. The same ratio (2.9) can be found when we divide the maximum uplift by the maximum subsidence resulting from the FE model. Thus, we use a simple relation, $\dot{q}_2 = 2.9\dot{q}_1$, to determine $\dot{q}_2$, and reduce the number of parameters to be estimated in Experiment 3.

Comparison of Experiment 3 to Experiments 1–2

Firstly, we investigate if we can get similar parameter estimates for the time-variant problem as the time-invariant problem (Experiments 1–2). We use the same synthetic data distributions as in Experiments 1–2: (1) evenly distributed data every 15 km, (2) only continental data and (3) continental- and near-trench data (see Fig. 7e for the data locations of the latter case). We start the assimilation at $t = 15.25\tau$. For the experiments with evenly distributed data and continental data only, we include data at all times during the assimilation. For the experiment with continental- and near-trench data we introduce near-trench data after 23 assimilation steps at $t = 18.125\tau$. For the evenly spaced data, estimates of the plate thickness and the two line load locations are similar to Experiments 1–2, but have smaller uncertainties (Tables 2 and 3). The plate thickness estimate excludes the truth more explicitly than before, that is the plate thickness is more precisely but inaccurately estimated. The estimates from Experiment 3 are more tightly constrained due to the larger amount of data and assimilation steps than in Experiments

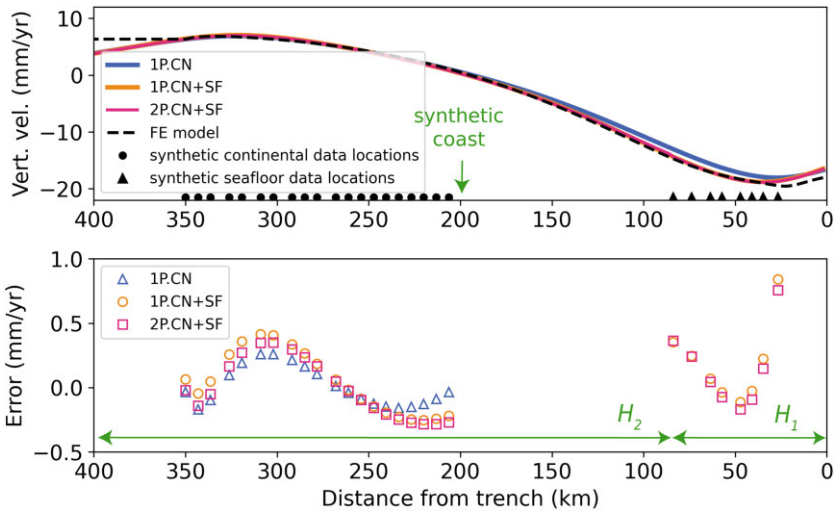

Figure 4. Assimilation results obtained for uniform plate (1P) and two-plate (2P) models with unevenly distributed data using a non-identical twin experiment (Experiment 1–2). The experiments with the 1P model either only use synthetic- continental data (1P.CN) or continental and seafloor data (1P.CN+SF) in the assimilation procedure. The 2P model experiments use continental and seafloor data (2P.CN+SF). The dotted lines show the FE model results and the black dots in the upper panel on the *x*-axis indicate the data locations. The estimated parameters are shown in Table 2.

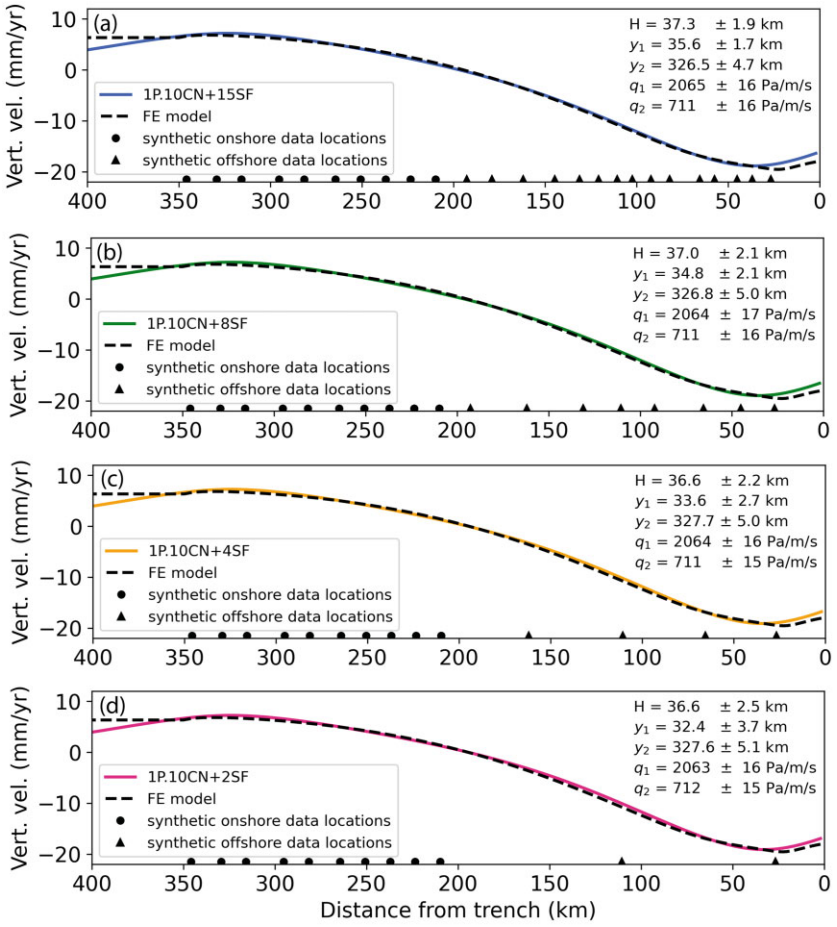

Figure 5. Assimilation results for the uniform plate model (1P) with different distributions of synthetic seafloor observation locations (Experiment 1). Each panel shows the weighted vertical velocities and lists the estimated model parameters and 1-standard deviation for different numbers of synthetic continental (CN) and seafloor (SF) data stations. For example, 1P.10CN+15SF in panel (a) means that 10 synthetic continental and 15 seafloor observations were used to calibrate the 1P model.

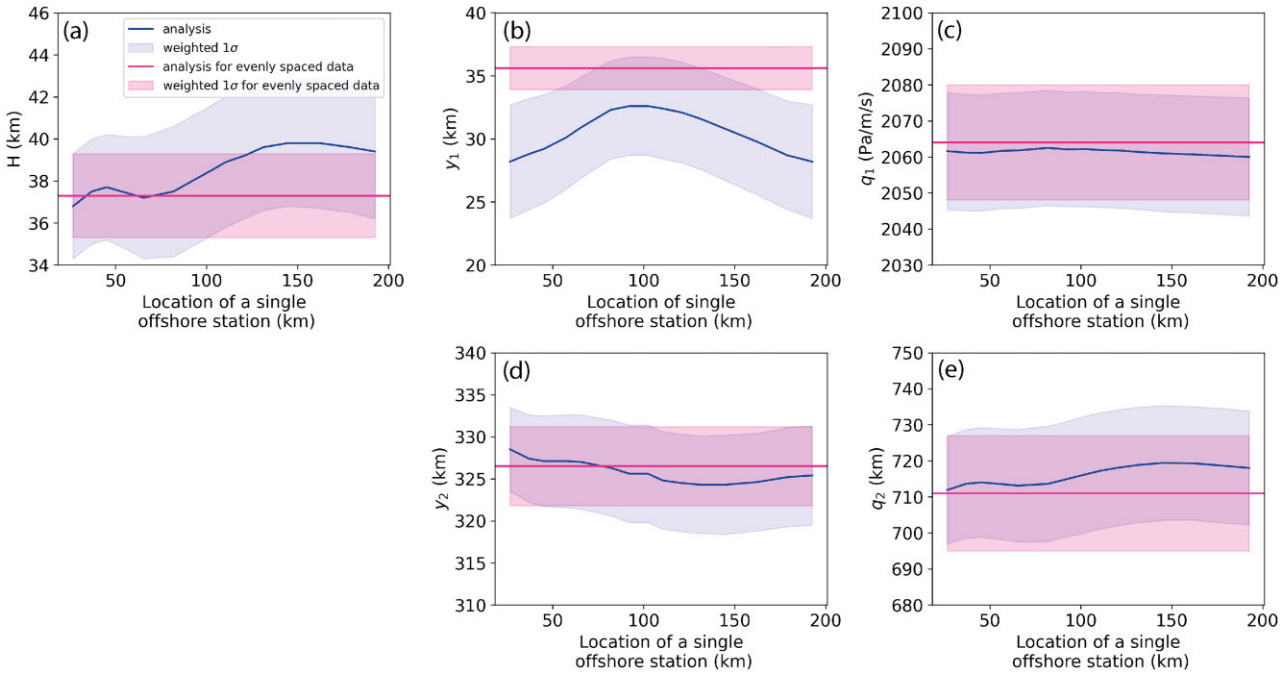

Figure 6. Assimilation results with 10 synthetic onshore data locations and one location for a synthetic seafloor data point, which we vary in the experiment, obtained with the uniform plate model (Experiment 1). Blue lines show the parameter results for the case where the location of the synthetic seafloor data point is varied. Pink lines show the estimated parameter results for the case where regularly distributed synthetic data in continent and ocean are used with a uniform plate model (shown in Table 2).

1–2. We note that the modelled displacements are remarkably similar to the FE model displacements and differences are smaller than 30 mm at the last time step where the accumulated deformation is approximately 100 cm for both the case where the data consists of synthetic continental- and near-trench data (Figs 7e and f) and for evenly spaced data (Figs S4e and f). If we exclude seafloor data and thus only feed continental data to the assimilation, then y_1 is near-zero, H and $\dot{q}_1$ are overestimated by more than 26 and 12 per cent, respectively, in comparison to the cases where seafloor data is used (Table 3). Moreover, when excluding seafloor data, we see that $\dot{q}_1$ and y_1 estimates increase steadily over time with a steadily decreasing y_2 (Fig. S5). Hence, the model parameters have not converged and cannot be well constrained with continental data only, similar to Experiment 1. Convergence occurs after approximately 15 out of 67 assimilation steps for evenly spaced data (Fig. S4) and after approximately 40 steps (only for the plate thickness) for continental data only (Fig. S5).

Influence and timing of synthetic seafloor data

In Japan, GNSS/A stations were later additions to the observation network. We analyse the effect of adding synthetic seafloor data to the assimilation process and how the timing of adding synthetic seafloor data influences the results. We start the assimilation again at $t = 15.25\tau$ with only continental data and add synthetic seafloor data after 23 assimilation steps at $t = 18.125\tau$ (see Fig. 7e for the data distribution). Up until $t = 18.125\tau$ we see a strongly increasing plate thickness, while the rate $\dot{q}_1$ slowly increases and y_1 shifts trench-ward, as no seafloor data is added up until this time (Figs 7b and d). y_1 reaches negative values, which shows that physically unrealistic combinations result in a good fit with the measured surface displacements (Fig. 7b). Once synthetic seafloor observations are added to the assimilation, all parameters converge towards different values (Figs 7a–d). The inclusion of seafloor data leads to convergence in the time-dependent tests with a slightly underestimated elastic plate thickness, similar to the time-independent tests with seafloor data. Notably, y_1 obtains a more realistic value (∼33 km, Fig. 7b, Table 3), which shows the added value of seafloor data. We repeated the experiment with evenly spaced data where synthetic seafloor data are added at the beginning of the assimilation process and obtained similar estimates (Table 3 and Fig. S4). The near-trench line load rate, $\dot{q}_1$, is also more tightly constrained by seafloor displacements than without seafloor data. In the case where no seafloor data is added (Fig. S5), the plate thickness estimate increases steadily over time with a steadily increasing line load rate magnitude, which again shows that the parameter y_1 cannot be well constrained with continental data only. The timing of adding seafloor data is also relevant for achieving convergence. Similar values for the plate thickness could be achieved if seafloor data is added before $t = 19.4\tau$ within the considered time (Fig. S6).

Influence of jittering magnitude

Jittering is applied after resampling to increase the spread of the particles (Section 2.2) and the value of the jitter is based on trial and error in this experiment. As done previously, we start the assimilation at $t = 15.25\tau$ with only continental data and add synthetic seafloor data after 23 assimilation steps at $t = 18.125\tau$. We start with a standard deviation of the jitter of 1, 2, 5 km and 3 Pa m^{-1} s^{-1}, for H, y_1, y_2 and $\dot{q}_1$, respectively. Large jitters can influence the posterior distribution. For example, the spread of y_1 is somewhat larger than in Experiments 1 and 2 (between 1.7 and 4.4 km in Experiments 1–2 and between 5.0 and 5.5 in Experiment 3, Tables 2 and 3), as a larger jitter was implemented to ensure that the data assimilation can correct the parameter estimation when seafloor data is added to the process. Particularly, for the parameters H, y_1 and y_2, the relatively

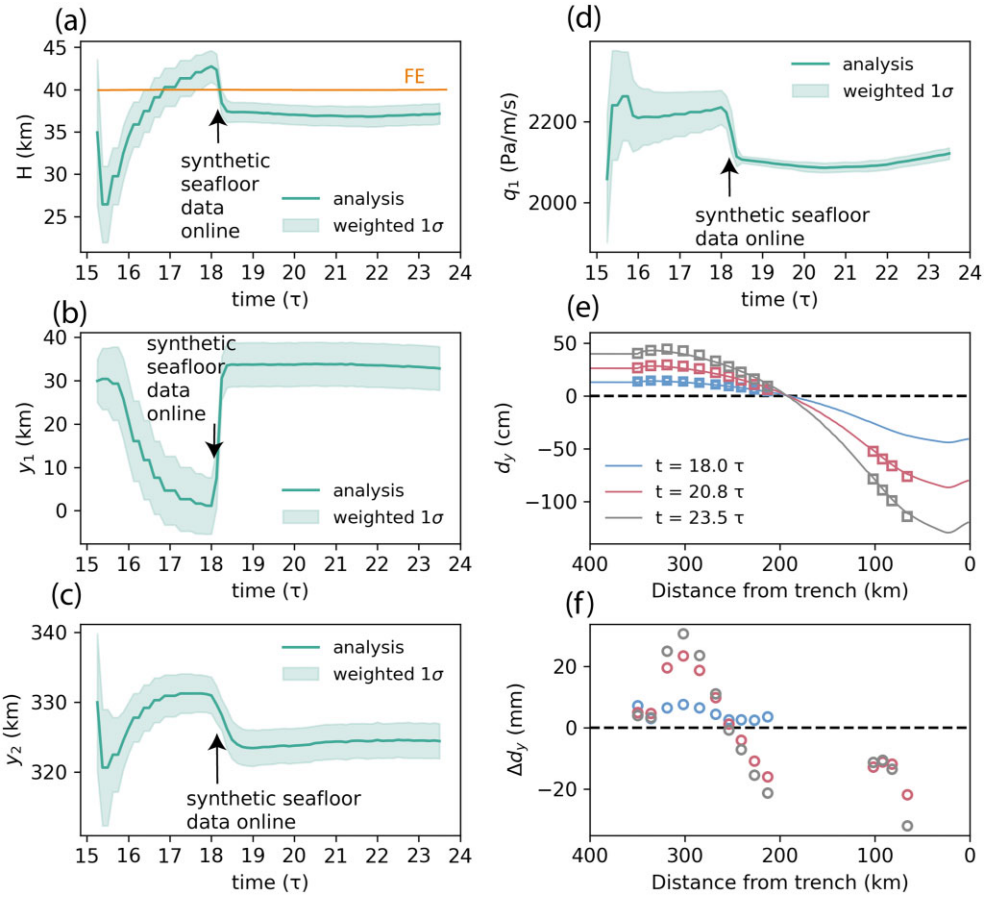

Figure 7. Evolution of model parameters estimates and uncertainties as a function of time (Experiment 3). Time is expressed as a multiple of the characteristic relaxation time τ. (a) plate thickness H, truth indicated by the orange line, (b) forearc line load location y_1, (c) backarc line load location y_2 and (d) line load rate magnitude $\dot{q}_1$. (e) displacements (d_y) of the FE model (solid lines) and the analysis (squares) at selected time steps. (f) differences (Δd_y) between the truth (FE model) and the analysis. At the start ($t = 15.25\tau$) only synthetic continental data are fed to the assimilation procedure. At $t = 18.125\tau$ synthetic seafloor data are added to the assimilation procedure.

Table 3. Assimilation results at the last time step for the time-dependent model with observations generated from a finite element model, with different data distributions (Experiment 3). See text for symbol definitions. The second line load rate, $\dot{q}_2$, is a function of $\dot{q}_1$: $\dot{q}_2 = 2.9\dot{q}_1$.

Data distribution	Experiment number	H (km)	y_1 (km)	y_2 (km)	$\dot{q}_1$ (Pa m^{-1} s^{-1})
Truth (FE model)	–	40.0	—	—	—
Evenly spaced (15 km)	3	36.7 ± 1.1	32.8 ± 2.1	323.0 ± 2.3	2122 ± 13
Only synthetic continental	3	46.8 ± 1.3	-0.2 ± 5.5	328.9 ± 2.4	2391 ± 23
Synthetic continental + near-trench	3	37.1 ± 1.2	32.8 ± 5.0	324.4 ± 2.5	2122 ± 14

large standard deviation of jittering (1, 2 and 5 km, respectively) influences the posterior distribution after synthetic seafloor data are added to the assimilation procedure (Fig. 8). When reducing the standard deviation of the jitter for y_1 to 1 km, the assimilation procedure is unable to sufficiently correct the parameter estimation and thus a bad fit is obtained at the synthetic seafloor locations (case 4 in Fig. S7). Similarly, when reducing the standard deviation of the jitter for H to 0.1 km, the assimilation procedure obtains a worse fit prior to the addition of synthetic seafloor data (case 2 in Fig. S7). Larger jitters are required for a good convergence of parameter estimates when synthetic seafloor data are added at a later time, at the expense of having a larger uncertainty of the posterior for H_1, y_1 and y_2 (case 1 in Fig. S7).

4.2 Identical twin experiments

4.2.1 Estimating lateral thickness variations from synthetic time-series (Experiment 4)

The FE model that constitutes the truth for the non-identical twin experiments that we considered thus far is limited to a uniform overriding plate thickness, except for the taper toward the trench. However, spatial variations in plate compliance (equivalent to thickness) can influence surface displacements (Itoh *et al.*2019, 2021). We therefore assess whether spatial variations in plate thickness can be retrieved from noisy data (Experiment 4, Table 1). We use eqs 11, 12 and 13 to describe the system and assimilate displacements. We use the same model to generate the synthetic data as the model that

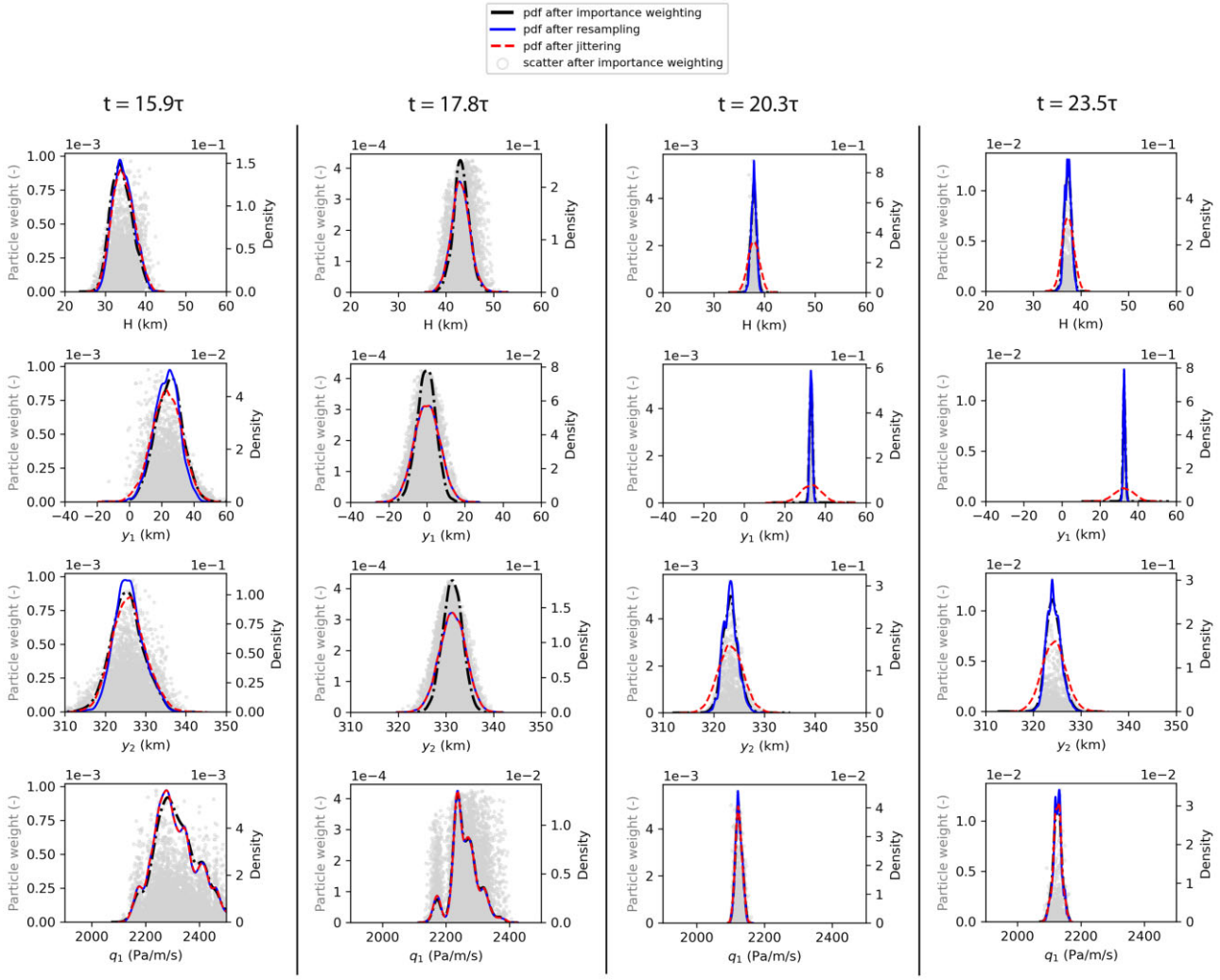

Figure 8. Scatter plots and posterior pdf plots for the plate thickness H, first line load location y_1, second line load location y_2 and line load rate magnitude $\dot{q}_1$ after importance weighting, resampling and jittering at select time steps (Experiment 3). Synthetic seafloor data is added after $t = 18.125\tau$ to the assimilation procedure. Note the scaling on the two y-axes for the particle weight and probability density. The evolution of each parameter is depicted in Fig. 7.

is used in the data assimilation in an identical twin experiment. In this model, the plate thickness varies spatially. Lateral variations are defined by a sine function, with the thickest plate (40 km) located ∼300 km from the trench, tapering to a normal thickness (30 km) at ∼80 km away from this welt. With data assimilation we aim to estimate the plate thickness deviations dH relative to the normal thickness of 30 km (Experiment 4, Table 1). The flexural model is set up in such a way that the choice of the plate thickness at a certain location only influences the model output at that same location. For our convenience, we discretize the plate thickness at the real GNSS locations with a 60 km swath (Figs 2a and c). The selection of the location of the plate thickness variation estimate is determined by the locations of the real GNSS stations, that is resulting in 16 variations of the plate thickness. The remaining parameters (line load locations and rate magnitudes) are fixed and thus we do not estimate them using the PF method. We sample independent surface displacements from the truth and add relatively small Gaussian noise with zero mean and standard deviation of 1 mm (i.e. the the standard deviation of the observation error) to all observations. Experiment 4 consists of 144 time/assimilation steps and each time step is 1 week.

The mean of the ensemble of models gives an estimate for the plate thickness after 3 yr that is close to the truth (Fig. 9a). Most of the differences between the mean and the truth vary between 3 and 8 per cent, whereas at one particular location at $x = 289$ km, a maximum error of the plate thickness of 19 per cent is obtained (Fig. 9b). Interestingly, the truth is captured by the ensemble spread at all observation locations (Fig. 9a). The ensemble spread is largest at ∼300 km from the trench and relatively large at the western and eastern coastlines (∼200 and ∼400 km from the trench) (Figs 9a and b). Also, a smaller distribution of particle weights is seen where a larger spread in dH is obtained (Fig. 9h), whereas this distribution is much broader when a smaller range of plate thicknesses is obtained (Fig. 9e, note the difference in scale on the x-axis). This means that a variety of plate thicknesses result in similar output displacements at locations where the displacements are small (of the same order as the observation uncertainty) which explains the narrower and broader widths of the density plots at $x = 245$ km and $x = 289$ km, respectively (Figs 9c and f). Additionally, parameter convergence is achieved at $x = 245$ km, where this is not the case for $x = 289$ km, which shows large oscillations (Figs 9d and g). Increasing the length of the time-series (up to 6 yr) did not reduce the

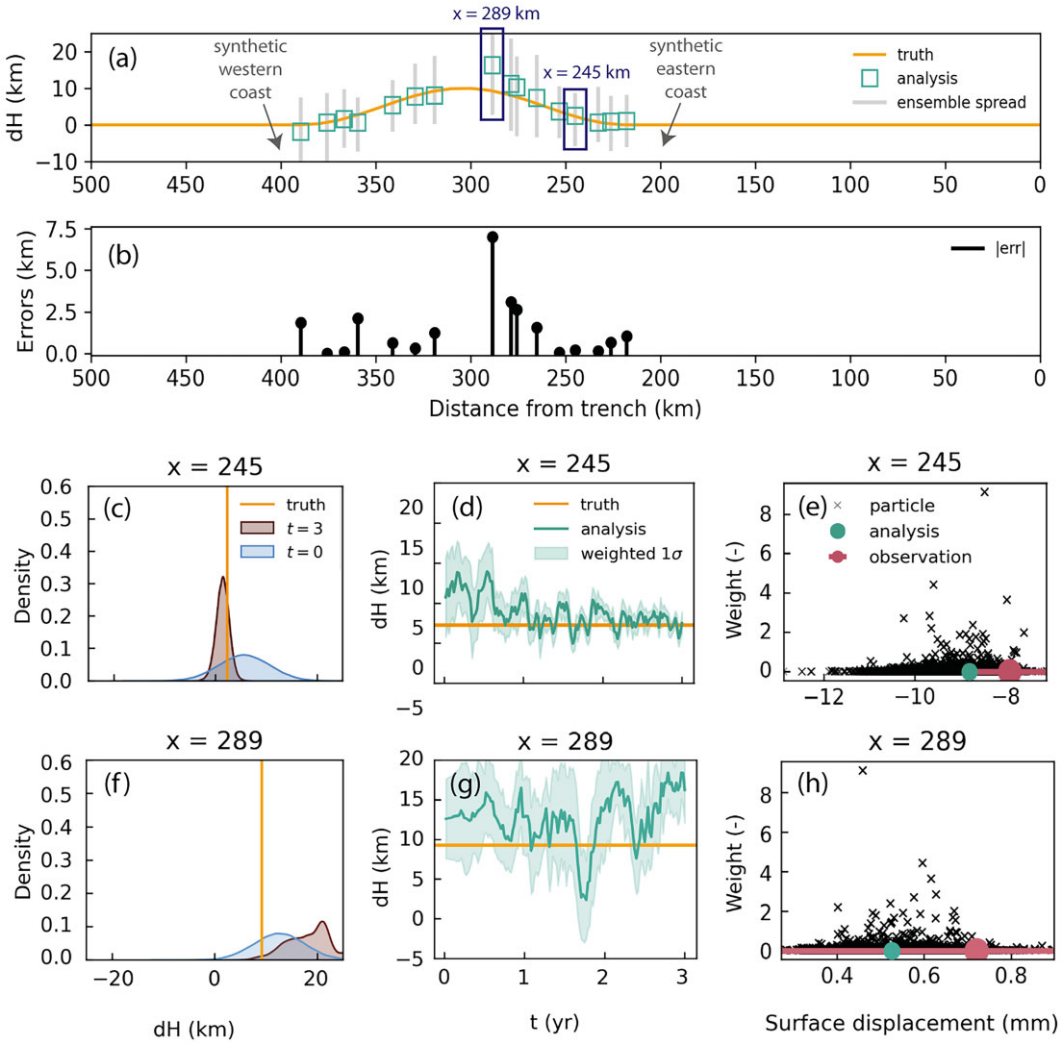

Figure 9. Time-dependent estimates of spatial variation in the overriding plate thickness using an identical twin experiment (Experiment 4). The number of particles is 100 000. (a) Deviation from a uniform plate thickness of 30 km; (b) absolute errors of the deviation in plate thickness; (c) density distribution of the plate thickness distribution at the start (blue, $t = 0$ yr) and at the end (purple, $t = 3$ yr) of the assimilation process at $x = 245$ km; (d) temporal evolution of the plate thickness deviation at $x = 245$ km; (e) particle weight versus vertical surface displacement at $x = 245$ km; (f) density distribution of the plate thickness distribution at the start (blue, $t = 0$ yr) and at the end (purple, $t = 3$ yr) of the assimilation process at $x = 289$ km; (g) temporal evolution of the plate thickness deviation at $x = 289$ km; (h) particle weight versus deformation at $x = 289$ km. Similar plots (c–h) at each station can be found in Figs S8–S10.

oscillations. How well the truth was captured at the end of the time-series depends on the oscillation and when the time-series is ended. Even though oscillations are high, the truth is captured within a 1σ or 2σ uncertainty at all stations (Figs 9d, g and S9).

4.2.2 Incorporating realistic representation errors (Experiment 5)

The vertical GNSS crustal observations are quite noisy (Fig. 2b) and contain signals from many different processes. However, our conceptual model only accounts for the semi-monotonous component in the observations. We account for the missing physics by incorporating time-varying representation errors in the data assimilation (as explained in Section 3.3). The representation error is the sum of the linear-, seasonal components, steps and common-mode error, which are derived from real GNSS observations (e.g. Fig. 2b). The representation error is assumed to be more realistic as they are derived empirically, instead of drawing the total observation error from a random distribution which renders more or less time-independent errors as in Experiments 1-4. We next investigate the data assimilation performance in identical twin Experiment 5 where noisy observations are mimicked by superimposing half of the representation error on the truth (Table 1) which generates the missing physics. The data distribution is taken identical to the case of real data, where only continental data is available (shown in Fig. 2a). We use eqs 11, 12 and 13 to describe the system and assimilate displacements. Experiment 5 consists of 994 assimilation steps and each time step is 1 day. Similar to Experiment 3 (Section 4.1.2), we only estimate the parameters H, y_1, y_2 and $\dot{q}_1$ using data assimilation and assume that $\dot{q}_2 = \dot{q}_1$. We based this on the notion that the magnitude for the maximum uplift is similar to the magnitude of maximum subsidence, as suggested by the data in Fig. 2c. Thereafter, the data assimilation is repeated with real observations (Experiment 6, Table 1).

Pilot tests reveal that different combinations of plate thickness and the line load rate magnitude lead to similar surface deformation

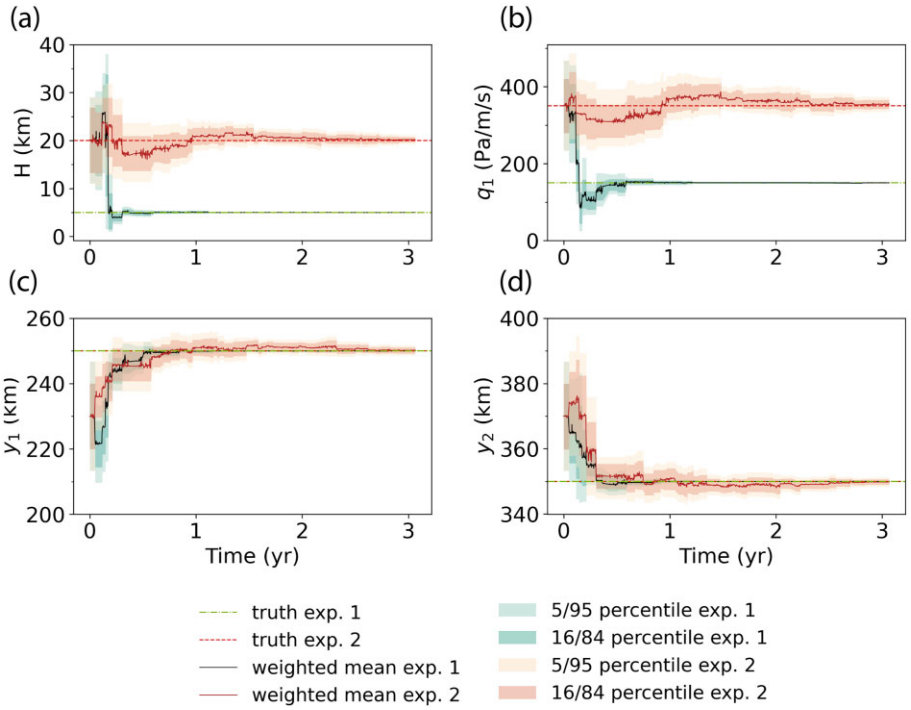

Figure 10. Time-series of the parameters (a) plate thickness H, (b) the line load rate magnitude $\dot{q}_1$, (c) the first line load location y_1 and (d) the second line load location y_2, obtained with the twin experiment (Experiment 5). The orange colours denote the long wavelength simulation in which $H_{\text{truth}} = 20$ km and $\dot{q}_{1_{\text{truth}}} = 350$ Pa m^{-1} s^{-1} (exp. 1) and the green colours denote the short wavelength simulation in which $H_{\text{truth}} = 5$ km and $\dot{q}_{1_{\text{truth}}} = 150$ Pa m^{-1} s^{-1} (exp. 2). In both cases, the true first- and second line locations are 250 and 350 km, respectively. The number of particles is 10 000.

values. We set up two experiments to investigate whether we can separate the plate thickness and rate magnitude from each other. The true values for the first experiment are $H_{\text{truth}} = 5$ km and $\dot{q}_{1_{\text{truth}}} = 150$ Pa m^{-1} s^{-1} (a short wavelength experiment) and for a second experiment $H_{\text{truth}} = 20$ km and $\dot{q}_{1_{\text{truth}}} = 350$ Pa m^{-1} s^{-1} (a long wavelength experiment). In both cases the true values of the other parameters are $y_{1_{\text{truth}}} = 250$ km and $y_{2_{\text{truth}}} = 350$ km. For the first experiment, we constrain H to be larger than 1 km to avoid extremely short wavelengths and unphysically negative H values. Specifically, we correct values lower than 1 km for the plate thickness right after the jittering step (Fig. 1b) to 1 km.

In both the low- and high wavelength experiments the parameters evolve towards the truth, even when the truth is outside the initial prior distribution (Figs 10a–d). The result of the long wavelength experiment shows larger uncertainties than the short wavelength experiment (see the spread of the time-series in Figs 10a–d), which is acceptable as wavelengths are larger and thus model outputs are less sensitive to changes in plate thickness. To understand the correlation between parameters over time, we create scatter plots at select time steps (Figs 11a–d). At the last time step we can observe that the long wavelength experiment has a wider range of plate thickness estimates than the short wavelength experiment (Figs 11a and c insets and blue kernel density plots). For both the short- and long wavelength simulations, the particles come closer to the truth over time, although quicker for the short wavelength case (in approximately 0.2 and 1.0 yr for the short- and long wavelength simulations, respectively, Fig. 10). There is a very strong correlation between the parameter pair H and $\dot{q}_1$ for the long wavelength case with a Pearson correlation of 0.90. The very strong correlation even at the end of the simulation indicates that there is a persistent trade-off between plate thickness and load line rate at such magnitudes. For the short wavelength case, the correlation drops to 0.40.

4.3 Assimilation of geodetic displacement time-series prior to the Tohoku-Oki earthquake (Experiment 6)

In a final set of data assimilation experiments (Experiment 6) we assimilate interseismic vertical displacements measured prior to the 2011 M_{w} 9.0 Tohoku-Oki earthquake (Section 3.1, Fig. 2). Just as in Experiment 5 (Section 4.2.2), we use eqs 11, 12 and 13 to describe the system, only estimate the parameters H, y_1, y_2 and $\dot{q}_1$ using data assimilation and assume that $\dot{q}_2 = \dot{q}_1$. We find that estimates of the effective elastic plate thickness across Tohoku between 3 and 7 km (Figs 12a and 13a) within a half swath width of 30 km (Fig. 2a). Increasing the half swath width to 50 km leads to similar estimates of the plate thickness between 5 and 10 km. Thus, we find that solutions for a relatively thin plate (low flexural rigidity and short wavelength) provide the best fit to real vertical displacement observations. Interestingly, slightly larger thicknesses of 5–7 km have a larger weight (inset in Fig. 12a) and thus give more accurate results (for both selections of the swath width). At the last time step, the correlation between H and $\dot{q}_1$ is 0.40, which is lower than the long wavelength case and equivalent to the short wavelength case in the twin experiments (Section 4.2.2). The plate thickness H converges to values well above the applied constraint of 1 km (Fig. 13). To achieve parameter convergence over time the constraint on a minimum effective elastic plate thickness is critical. Upon removal of the constraint $H > 1$ km, unphysical negative H values are obtained. Without applying additional constraints, no parameter convergence can be achieved.

The resulting estimates of the other parameters are such, that a low plate thickness is always obtained. The remaining parameters converge as well and the uncertainty of each parameter reduces over time (Fig. 13). The uncertainty values for the second line load

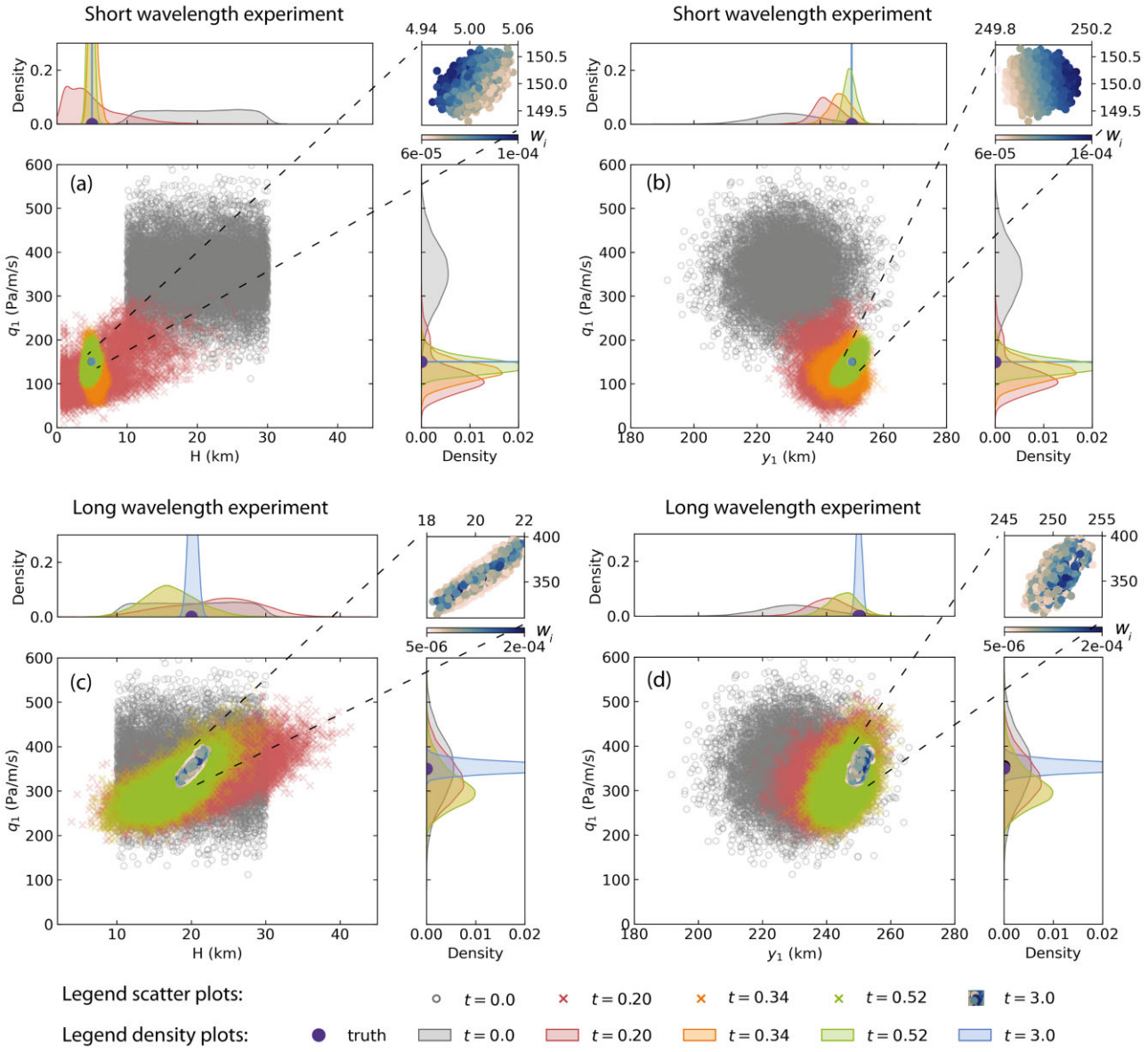

Figure 11. Scatter and kernel density plots of (a, c) the plate thickness H and line load rate magnitude $\dot{q}_1$ and (b, d) the first line load location y_1 and line load rate magnitude $\dot{q}_1$ at various time steps with synthetic data using an identical twin experiment (Experiment 5). (a, b) diagrams resulting from the short wavelength simulation and (c, d) diagrams resulting from the long wavelength simulation. In plots (a) and (b) the posterior density at $t = 3$ yr (i.e. the end of the simulation) is almost a straight line visually, given the scaling. The insets show the distribution of the particles at the end of the simulation ($t = 3$ yr) with their weight, w_i, denoted with colours.

location (373 ± 2 km) are approximately two times larger than that of the first-line location (257 ± 1 km), because fewer observations are available farther away from the trench in comparison to the eastern coast (Fig. S11).

Experiments with synthetic observations sampled from the FE model of Govers *et al.* (2018) show that the plate thickness converged towards the truth only upon the addition of seafloor data (Experiment 3, Fig. 7). Our identical twin experiments with continental data only and real representation errors also show convergence towards the truth for short- and long wavelength solutions (Fig. 10). However, when we run our identical twin experiment with a true plate thickness of 40 km, convergence cannot be achieved with continental data only. Similar values for the plate thickness around 40 km result in similar model outputs where GNSS stations are located (between 200 approximately 200 and 400 km from the trench). Therefore, it becomes difficult to constrain the plate thickness for long wavelength solutions when only continental data is used. The absence of accurate convergence using a higher true plate thickness confirms that additional information, for example in the form of seafloor data, is required for the real experiments to accurately constrain model parameters of the conceptual model. However, we find low wavelength estimates (5–7 km) to explain the continental data, and thus convergence has been achieved without seafloor data. Even when excluding four continental data points closest to the trench that suggest little subsidence or even uplift (Fig. 2), similarly low estimates of the plate thickness are obtained.

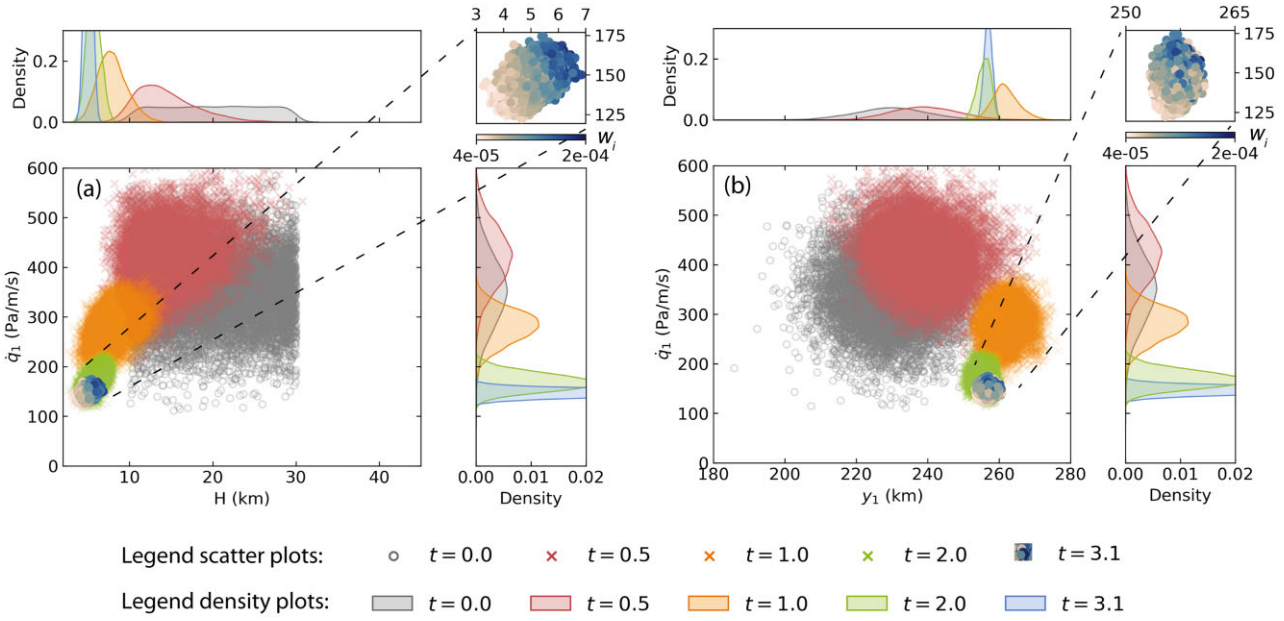

Figure 12. Scatter and kernel density plots of (a) the plate thickness H and line load rate magnitude $\dot{q}_1$ and (b) the first line load location y_1 and line load rate magnitude $\dot{q}_1$, estimated at various time steps from real data prior to the 2011 M_w 9.0 Tohoku-Oki earthquake (Experiment 6). The grey, red, orange and green colours denote the distribution at $t = 0$, $t = 0.5$, $t = 1.0$, $t = 2.0$ yr after 1 January 1997. The blue-coloured densities are the posterior densities at $t = 3.1$ yr after 1 January 1997 (i.e. the end of the simulation). The inset shows the distribution of the particles with their weight, w_i, denoted with yellow and blue colours.

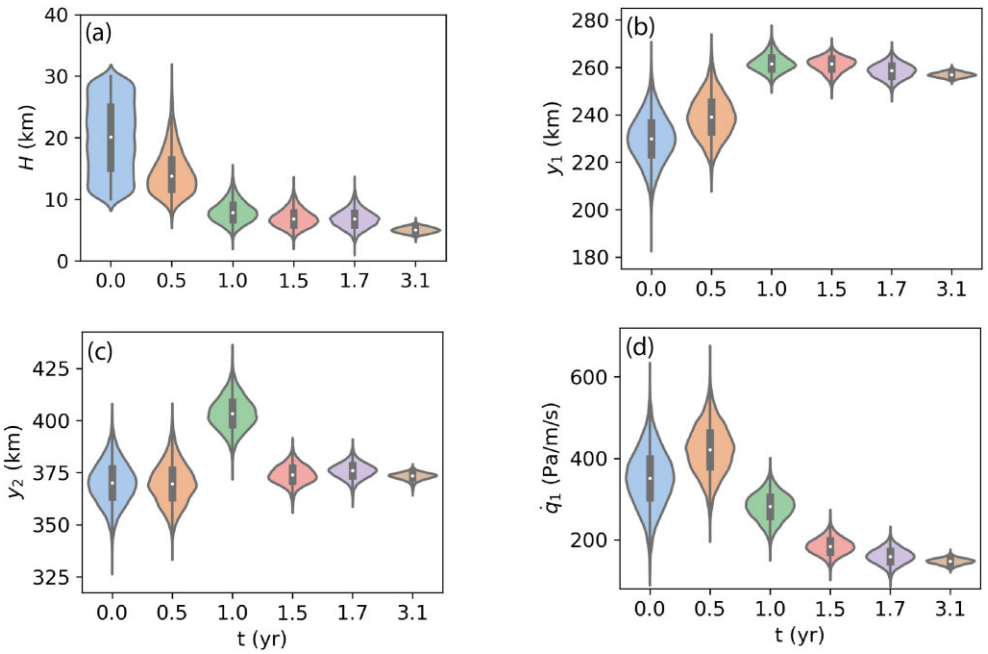

Figure 13. Violin plots depicting estimates of (a) plate thickness H, (b) first line load location y_1, (c) second line load location y_2 and (d) first line load rate magnitude $\dot{q}_1$ at selected times using real data prior to the Tohoku-Oki earthquake (Experiment 6). The curved line of each violin plot is the kernel density function, the white dot represents the median, the thick black line represents the data values between the first and third quartiles, and the edges of the thin black line are the lower and upper adjacent values.

5 DISCUSSION

5.1 Exploring the use of data assimilation

5.1.1 Prior selection and imposing constraints

An advantage of Bayesian-based data assimilation methods is that the truth can be recovered even when the chosen prior at the first time step does not include the truth as demonstrated in Experiment 5 (Fig. 10). This is highly advantageous when there is little to no knowledge on the parameter range. This becomes visible when new data are being assimilated and the evolution of our estimate is effectively steered towards the truth, provided that we apply a jitter that is large enough (Experiment 3, Fig. 7). In some cases, constraints on the parameters are necessary, such as in Experiments 5 and 6.

We had to impose a minimum plate thickness of 1 km to avoid the data assimilation to estimate unphysically negative values for the plate thickness while not introducing a bias to the estimation. To test whether our choice of prior thickness induced this behaviour, we ran additional simulations where we selected a prior at the beginning of the simulation to be closer to or containing the true plate thickness. A narrow prior at the beginning of the simulation did not lead to negative values of the plate thickness (Fig. S12d). However, when the prior at the beginning of the simulation is broader, or biased, negative values are obtained for the plate thickness (Figs S12a–c). This suggests that the negative values of our plate thickness estimates result from an overshoot due to a large ensemble variance needed for the initial correction, to effectively steer the evolution of the plate thickness estimate towards the truth when the selected prior is far from the truth.

5.1.2 Addressing missing physics

The conceptual model lacks some key physical processes that affect vertical displacements in subduction zones. Particularly, the kinematic description in terms of vertical line loads seems not to represent the governing physical processes well, as these are anticipated to result from horizontal compression during the interseismic period. Moreover, the model does not account for a dipping, curved megathrust interface, an accurate viscoelastic response of the mantle wedge and oceanic lithospheric mantle, as well as viscoelastic vertical layering and horizontal variation in compliance in the overriding plate (e.g. lithological stratification imposing a backstop). Several of these missing processes are anticipated to shorten surface displacement wavelengths van Dinther *et al.* (2019), as required by our results. Instead of implicitly dealing with the model error as part of the observation error, model errors can also be estimated explicitly by including model errors in the state vector as an additive variable to the total deformation in eq. 12. In our current setup, the plate thickness and line load rate magnitude parameters are strongly coupled (Fig. 11c), and this directly influences the ill-posedness of the estimation problem. We tested a setup with model errors included in our state vector and obtained solutions with near-zero model deformation outputs whilst model errors were fitted to the data (Fig. S13). Adding the model error to the state vector would consequently lead to a stronger ill-posedness of the estimation problem. Dealing with the estimation of model errors through data assimilation will be part of our future research.

5.1.3 Data assimilation for more complex models

One of the potential drawbacks of the particle filter is that the computational time increases with the number of unknowns. The number of particles required to avoid particle degeneracy increases exponentially with the dimensionality of the problem (Snyder *et al.*2008). In this paper we use a model that requires very little computational time, which makes the propagation step computationally inexpensive. In Experiments 1–4 we required 10 000 particles to estimate 4–6 parameters in several minutes on a Quad-core Core i7 machine. Increasing the dimension of the problem to 16 (Experiment 4) required 100 000 particles and increased the execution time tenfold. In more complex models with more unknown parameters or state variables, more particles are required to avoid ensemble degeneracy (Snyder *et al.*2008). For example, with 10^5–10^6 number of unknowns, the execution time would roughly increase by more than 10^4 times. In the example of Snyder *et al.* (2008), 10^{11} particles are required for a number of unknowns of 200. More realistic tectonic models require more computational costs and exploiting parallelism in multicore or multithreading architectures and considering other data assimilation methods becomes important. Suitable alternative solutions for parameter estimation to achieve that include ensemble methods such as the Ensemble Smoother-Multiple Data Assimilation (ES-MDA; Emerick & Reynolds 2013). These methods may be effective with a distinctly smaller number of realisations than required for a particle filter. This reduces computational effort at the expense of the ability to accurately deal with strongly non-Gaussian error distributions. For strongly non-linear processes, the particle flow filter (Hu & van Leeuwen 2021) could be an alternative worth exploring.

5.2 Importance of seafloor data

Our results highlight the added value of seafloor data in estimating model parameters from vertical surface deformation. Particularly, once synthetic seafloor data is added to the non-identical twin experiment, a quick convergence is seen to parameter estimates closer to the truth (Figs 7a and e). The addition of seafloor data effectively steers the evolution of the forecast and results in a smaller spread of the posterior ensemble and a smaller misfit of its mean with the truth than was the case for the prior ensemble. The optimal position of the synthetic seafloor data is within 150 km from the trench to ensure satisfactory convergence of the plate thickness and first line load location estimates (Fig. 6). Note that the accuracy of the seafloor observations in our synthetic simulations is taken to be similar to that of on-land observations. In our real-data experiments we did not use seafloor data as this was not available during our studied period and we could obtain convergence for our short wavelength solutions. Nevertheless, seafloor data can provide additional constraints.

However, there are some limitations to the applicability of actual seafloor data in data assimilation procedures due to the accuracy and timing of the data. In northeast Japan, seafloor stations MYGI (∼100 km from the trench) and MYGW (∼150 km from the trench) are located within our swath (Fig. 2a) and show an interseismic linear signal of 2.0 ± 2.1 and -0.2 ± 3.3 cm yr^{-1} (95 per cent confidence), respectively (Watanabe *et al.*2021). However, seafloor data contain larger measurement uncertainties than on-land data, such that the likelihood is lower and the PF method assigns a lower weight to the seafloor observations. We test the effect of adding two seafloor observations using the same setup as Experiment 6. We computed crustal seafloor displacements using the velocity values for stations MYGI and MYGW (2.0 and -0.2 cm yr^{-1}, respectively, Watanabe *et al.* (2021) and assume a standard deviation of 7.0 cm for the uncertainty (Iinuma *et al.*2021). However, our *a posteriori* estimate generally does not change, indicating that low accuracy seafloor data does not add much value. We also varied the seafloor observation uncertainty in our synthetic tests (Experiment 5). According to the synthetic tests, a maximum uncertainty of 28 mm is required for seafloor data when we assume a 4 mm uncertainty for our continental data to obtain similar model realizations if we assume 4 mm for both data types. Additionally, the available seafloor data came online in the mid-2007s, whereas we selected GNSS data between 1997 and 2000. GNSS data including the mid-2007s must be filtered (which may not be straightforward) to remove co- and post-seismic signals from various $M_w \sim 6$–7 megathrust earthquakes in the region for data consistency. Therefore, filtering co- and post-seismic signals should be considered when combining seafloor and onland data prior to the Tohoku-Oki earthquake.

5.3 Elastic thickness estimates

The data assimilation in this study renders relatively low values for the effective elastic thickness between 5 and 7 km (Experiment 6). Estimates of the effective elastic thickness from other studies vary from values as low as 3–10 km up to 50 km (Huang *et al.*1998; Kudo *et al.*2001; Muto 2011). To understand how these values compare, we need to consider that the effective elastic thickness of the lithosphere can be defined by various criteria, which can be based on the seismogenic layer (Maggi *et al.*2000), topography and gravity anomalies (Kudo *et al.*2001), thermo-rheological models (Tesauro *et al.*2013) and bending moment of the lithosphere (Burov & Diament 1995). The continental effective elastic thickness is considered to be dependent on the composition and thickness of the upper and lower crust and its geotherm (Burov & Diament 1995). The effective elastic thickness can help to understand (lateral) changes in rheology and temperature. Low seismic velocities and high seismic attenuation inferred beneath the volcanic arc of Northeast Japan (Wang & Zhao 2005; Liu *et al.*2014) are indicative of mechanically weak materials in and below the lower crust (Ohzono *et al.*2013) and thus a localized lower effective elastic thickness. Viscosity maps by Muto (2011) based on heat flow, seismic tomography, and magnetotelluric data suggest that the (laterally varying) effective elastic thickness on time scales of the earthquake cycle should be between 15 and 25 km. Our estimates are consistent with values inferred from topography and gravity anomalies in Northeast Japan (3–10 km) (Kudo *et al.*2001). Viscoelastic materials behave predominantly viscous on larger time scales and the viscosity decreases with depth. Therefore, the effective elastic plate thickness is expected to decrease over larger time scales. Considering the shorter time scales in our estimation problem, our estimates for the effective elastic thickness should have been larger than that of Kudo *et al.* (2001). Huang *et al.* (1998) find effective elastic thicknesses across Northeast Japan between 10 and 50 km based on long-term subduction modelling, which are higher than our estimates. Mechanical subduction earthquake models typically assume a thicker elastic plate where the bottom of the overriding plate coincides with the downdip of the seismogenic zone. In mechanical models where a uniform elastic plate is underlain by a viscous mantle, the effective elastic thickness (i.e. the elastic plate thickness) is between 40 and 50 km for Tohoku (Diao *et al.*2013; Yamagiwa *et al.*2015; Hu *et al.*2016). The compliance of the upper plate has gained some attention in the last years in mechanical models. The addition of a cold nose (i.e., essentially an elastic forearc) would subsequently reduce the overriding plate thickness in the backarc to match observations (Luo & Wang 2021). Using a cold nose often requires a thinner effective elastic thickness past the cold nose of the order 25–30 km (e.g. Sun *et al.*2014; Fukuda & Johnson 2021; Luo & Wang 2021). Itoh *et al.* (2019) show that compliance in the overriding plate in the volcanic arc and backarc in Hokkaido is needed to match interseismic geodetic observations. They found a plate thickness of 25, 2.5 and 10 km in the forearc, volcanic arc, and backarc, respectively, of which the latter two values are consistent with our estimated values.

6 CONCLUSIONS

The identical twin experiments show remarkable convergence towards the true model parameters using simulated GNSS data, even when we assume realistic observation errors, for short- and long wavelength solutions. In the non-identical twin experiments using data from a finite element subduction model, the addition of synthetic seafloor data appears to be instrumental to constrain model parameters well for long wavelength solutions. Our assimilation of GNSS data prior to the 2011 Tohoku-Oki earthquake (1997–2000) converges to unrealistically low estimates of the effective elastic thickness of the overriding plate of 5–7 km. Interestingly, trade-offs in parameter values are identified with twin experiments, particularly the overriding plate thickness and line load rate magnitude show a strong correlation.

Overall, our results demonstrate the feasibility and potential benefits of combining observations with dynamical models using the particle method. We illustrate how data assimilation can estimate model parameters and uncertainty values, how it can provide insights into the data-network sensitivity, and how it can identify and quantify trade-offs between parameter values.

INDEX AND SYNONYMS

Term	Synonym(s)	Defined in
Analysis step	Update step	Section 2.1, Section 2.2
Ensemble collapse	Particle degeneracy, filter degeneracy	Section 2.1, Section 2.2
Ensemble members	Particles, samples	Section 2.1
Importance weight	Particle weight	Section 2.2
Filter degeneracy	Particle degeneracy, ensemble collapse	Section 2.1, Section 2.2
Forecast step	Propagation step	Section 2.1, Section 2.2
Particles	Ensemble members, samples	Section 2.1
Particle degeneracy	Ensemble collapse, filter degeneracy	Section 2.1, Section 2.2
Particle weight	Importance weight	Section 2.2
Propagation step	Forecast step	Section 2.1, Section 2.2
Representation error	Representativeness error	Section 2.1, Section 3.3
Representativeness error	Representation error	Section 2.1, Section 3.3
Samples	Ensemble members, particles	Section 2.1
Update step	Analysis step	Section 2.1, Section 2.2

ACKNOWLEDGMENTS

The authors thank the editor Bertrand Rouet-Leduc, Byung-Dal So and an anonymous reviewer for their thoughtful comments and constructive criticism which helped us to improve this paper. This work was funded by the Dutch Research Council NWO grant ALWGO.2019.001. Author contributions following the CReDiT taxonomy: Conceptualization: RG, FV, CM, YvD; Data Curation: CM; Investigation: CM; Methodology: CM and FV; Resources and Software: CM; Validation: CM; Supervision: RG and FV; Visualization: CM; Writing-original draft: CM, RG, FV; Writing-review and editing: CM, RG, FV, YvD; Project Administration: RG. Funding Acquisition: RG.

DATA AVAILABILITY STATEMENT

Input and output files that were used for the models of this paper are digitally stored in the Yoda repository of Utrecht University and are accessible in compliance with FAIR (Findable, Accessible, Interoperable, Reusable) principles (doi:10.24416/UU01-1082KX). The GNSS displacements used in this study are available upon request at https://www.gsi.go.jp/ENGLISH/geonet_english.html, subject to the policies of the Geospatial Information Authority of Japan. Generic Mapping Tools (https://www. generic-mapping-tools.org/) were used to prepare the map in Fig. 2.

SUPPORTING INFORMATION

Supplementary data are available at *GJI* online.

suppl_data

Please note: Oxford University Press is not responsible for the content or functionality of any supporting materials supplied by the authors. Any queries (other than missing material) should be directed to the corresponding author for the paper.

REFERENCES

Altamimi, Z., Collilieux, X. & Métivier, L., 2011. ITRF2008: an improved solution of the international terrestrial reference frame, *J. Geod.,* **85**(8), 457–473.

Avouac, J.-P., 2015. From geodetic imaging of seismic and aseismic fault slip to dynamic modeling of the seismic cycle, *Ann. Rev. Earth planet. Sci.,* **43**(1), 233–271.

Banerjee, A., van Dinther, Y. & Vossepoel, F.C., 2023. On parameter bias in earthquake sequence models using data assimilation, *Nonlin. Proc. Geophys.,* **30,** 101–115. https://doi.org/10.5194/npg-30-101-2023.

Baumann, T. & Kaus, B.J., 2015. Geodynamic inversion to constrain the non-linear rheology of the lithosphere, *J. geophys. Int.,* **202**(2), 1289–1316.

Baumann, T., Kaus, B. & Popov, A., 2014. Constraining effective rheology through parallel joint geodynamic inversion, *Tectonophysics,* **631,** 197–211.

Benavente, R., Dettmer, J., Cummins, P.R. & Sambridge, M., 2019. Efficient Bayesian uncertainty estimation in linear finite fault inversion with positivity constraints by employing a log-normal prior, *J. geophys. Int.,* **217**(1), 469–484.

Bock, Y. *et al.*, 1997. Southern California permanent GPS geodetic array: continuous measurements of regional crustal deformation between the 1992 Landers and 1994 Northridge earthquakes, *J. geophys. Res.,* **102**(B8), 18 013–18 033.

Bunge, H.-P., Hagelberg, C.R. & Travis, B.J., 2003. Mantle circulation models with variational data assimilation: inferring past mantle flow and structure from plate motion histories and seismic tomography, *J. geophys. Int.,* **152**(2), 280–301.

Burov, E.B. & Diament, M., 1995. The effective elastic thickness (Te) of continental lithosphere: what does it really mean?, *J. geophys. Res.,* **100**(B3), 3905–3927.

Carrassi, A., Bocquet, M., Bertino, L. & Evensen, G., 2018. Data assimilation in the geosciences: an overview of methods, issues, and perspectives, *WIREs Clim. Change,* **9**(5), e535, doi:10.1002/wcc.535.

Cohen, S.C., 1999. Numerical models of crustal deformation in seismic zones, *Adv. Geophys.,* **41,** 133–231.

Dal Zilio, L., Jolivet, R. & van Dinther, Y., 2020. Segmentation of the Main Himalayan Thrust illuminated by Bayesian inference of interseismic coupling, *Geophys. Res. Lett.,* **47**(4), e2019GL086424, doi:10.1029/2019GL086424.

Diao, F., Xiong, X., Wang, R., Zheng, Y., Walter, T.R., Weng, H. & Li, J., 2013. Overlapping post-seismic deformation processes: afterslip and viscoelastic relaxation following the 2011 Mw 9.0 Tohoku (Japan) earthquake, *J. geophys. Int.,* **196**(1), 218–229.

Dong, D., Fang, P., Bock, Y., Webb, F., Prawirodirdjo, L., Kedar, S. & Jamason, P., 2006. Spatiotemporal filtering using principal component analysis and Karhunen-Loeve expansion approaches for regional GPS network analysis, *J. geophys. Res.,* **111**(B3), doi:10.1029/2005JB003806.

Douc, R. & Cappe, O., 2005. Comparison of resampling schemes for particle filtering, in *Proceedings of the 4th International Symposium on Image and Signal Processing and Analysis,* ISPA 2005, pp. 64–69.

Doucet, A. & Johansen, A., 2011. A tutorial on particle filtering and smoothing: fifteen years later, in *Oxford Handbook of Nonlinear Filtering,* pp. 656–704, eds Crisan, D. & Rozovskii, B., Oxford Univ. Press.

Duputel, Z. *et al.*, 2015. The Iquique earthquake sequence of April 2014: Bayesian modeling accounting for prediction uncertainty, *Geophys. Res. Lett.,* **42**(19), 7949–7957.

Emerick, A.A. & Reynolds, A.C., 2013. Ensemble smoother with multiple data assimilation, *Comp. Geosci.,* **55,** 3–15.

Evensen, G., 1994. Sequential data assimilation with a nonlinear quasi-geostrophic model using Monte Carlo methods to forecast error statistics, *J. geophys. Res.,* **99**(C5), 10 143–10 162.

Evensen, G., 2019. Accounting for model errors in iterative ensemble smoothers, *Comput. Geosci.,* **23,** 761–775.

Evensen, G., Vossepoel, F.C. & van Leeuwen, P.J., 2022. *Data Assimilation Fundamentals, A Unified Formulation for State and Parameter Estimation,* Springer Cham.

Fichtner, A., 2011. *Full Seismic Waveform Modelling and Inversion,* Springer-Verlag.

Freed, A.M., Hashima, A., Becker, T.W., Okaya, D.A., Sato, H. & Hatanaka, Y., 2017. Resolving depth-dependent subduction zone viscosity and afterslip from postseismic displacements following the 2011 Tohoku-oki, Japan earthquake, *Earth planet. Sci. Lett.,* **459,** 279–290.

Fukuda, J. & Johnson, K.M., 2008. A fully Bayesian inversion for spatial distribution of fault slip with objective smoothing, *Bull. seism. Soc. Am.,* **98**(3), 1128–1146.

Fukuda, J. & Johnson, K.M., 2021. Bayesian inversion for a stress-driven model of afterslip and viscoelastic relaxation: method and application to postseismic deformation following the 2011 Mw 9.0 Tohoku-Oki earthquake, *J. geophys. Res.,* **126**(5), e2020JB021620, doi:10.1029/2020JB021620.

Fukuda, J., Higuchi, T., Miyazaki, S. & Kato, T., 2004. A new approach to time-dependent inversion of geodetic data using a Monte Carlo mixture Kalman filter, *J. geophys. Int.,* **159**(1), 17–39 .

Fukuda, J., Miyazaki, S., Higuchi, T. & Kato, T., 2008. Geodetic inversion for space-time distribution of fault slip with time-varying smoothing regularization, *J. geophys. Int.,* **173**(1), 25–48.

Fukuda, J., Johnson, K.M., Larson, K.M. & Miyazaki, S., 2009. Fault friction parameters inferred from the early stages of afterslip following the 2003 Tokachi-Oki earthquake, *J. geophys. Res.,* **114**(B4), doi:10.1029/2008JB006166.

Gerya, T., 2022. Numerical modeling of subduction: State of the art and future directions, *Geosphere,* **18**(2), 503–561.

Gordon, N., Salmond, D. & Smith, A., 1993. Novel approach to nonlinear/non-Gaussian Bayesian state estimation, *IEE Proc. F (Radar and Signal Processing),* **140**(6), 107–113.

Govers, R. & Wortel, M., 1993. Initiation of asymmetric extension in continental lithosphere, *Tectonophysics,* **223**(1), 75–96.

Govers, R., Furlong, K.P., van de Wiel, L., Herman, M.W. & Broerse, T., 2018. The geodetic signature of the earthquake cycle at subduction zones: Model constraints on the deep processes, *Rev. Geophys.,* **56**(1), 6–49.

Hamada, N., 2000. Recent seismic activity in the Miyakejima and Niijima-Kozushima region, Japan -the largest earthquake swarm ever recorded-, *Earth Planets Space,* **52,** i–viii.

Herman, M.W. & Govers, R., 2020. Locating fully locked asperities along the south america subduction megathrust: a new physical interseismic inversion approach in a Bayesian framework, *Geochem. Geophys. Geosyst.,* **21**(8), e2020GC009063, doi:10.1029/2020GC009063.

Hirahara, K. & Nishikiori, K., 2019. Estimation of frictional properties and slip evolution on a long-term slow slip event fault with the ensemble

Kalman filter: numerical experiments, *J. geophys. Int.,* **219**(3), 2074–2096.
Hu, C. & van Leeuwen, P., 2021. A particle flow filter for high-dimensional system applications, *Quart. J. R. Meteorol. Soc.,* **147**(737), 2352–2374.
Hu, Y., Bürgmann, R. & Freymueller, J., 2014. Contributions of poroelastic rebound and a weak volcanic arc to the postseismic deformation of the 2011 Tohoku earthquake, *Earth Planet Space,* **66**(106), doi:10.1186/1880-5981-66-106.
Hu, Y., Bürgmann, R., Uchida, N., Banerjee, P. & Freymueller, J.T., 2016. Stress-driven relaxation of heterogeneous upper mantle and time-dependent afterslip following the 2011 Tohoku earthquake, *J. geophys. Res.,* **121**(1), 385–411.
Huang, S., Selwyn Sacks, I. & Arthur Snoke, J., 1998. Compressional deformation of island-arc lithosphere in northeastern Japan resulting from long-term subduction-related tectonic forces: finite-element modeling, *Tectonophysics,* **287**(1), 43–58.
Iinuma, T., Kido, M., Ohta, Y., Fukuda, T., Tomita, F. & Ueki, I., 2021. GNSS-acoustic observations of seafloor crustal deformation using a wave glider, *Front. Earth Sci.,* **9,** doi:10.3389/feart.2021.600946.
Itoh, Y., Wang, K., Nishimura, T. & He, J., 2019. Compliant volcanic arc and backarc crust in Southern Kurile suggested by interseismic geodetic deformation, *Geophys. Res. Lett.,* **46**(21), 11 790–11 798.
Itoh, Y., Nishimura, T., Wang, K. & He, J., 2021. New megathrust locking model for the Southern Kurile subduction zone incorporating viscoelastic relaxation and non-uniform compliance of upper plate, *J. geophys. Res.,* **126**(5), e2020JB019981, doi:10.1029/2020JB019981.
Janjić, T. *et al.*, 2017. On the representation error in data assimilation, *Quart. J. R. Meteorol. Soc.,* **144**(713), 1257–1278.
Jolivet, R., Simons, M., Agram, P.S., Duputel, Z. & Shen, Z.-K., 2015. Aseismic slip and seismogenic coupling along the central San Andreas fault, *Geophys. Res. Lett.,* **42**(2), 297–306.
Kano, M., Miyazaki, S. & Ito, K., 2013. An adjoint data assimilation method for optimizing frictional parameters on the afterslip area, *Earth Planets Space,* **65,** 1575–1580.
Kano, M., Miyazaki, S., Ishikawa, Y., Hiyoshi, Y., Ito, K. & Hirahara, K., 2015. Real data assimilation for optimization of frictional parameters and prediction of afterslip in the 2003 Tokachi-Oki earthquake inferred from slip velocity by an adjoint method, *J. geophys. Int.,* **203**(1), 646–663.
Kano, M., Miyazaki, S. & Ishikawa, Y., 2020. Adjoint-based direct data assimilation of GNSS time-series for optimizing frictional parameters and predicting postseismic deformation following the 2003 Tokachi-Oki earthquake, *Earth Planets Space,* **72**(159), doi:10.1186/s40623-020-01293-0.
Klein, E., Fleitout, L., Vigny, C. & Garaud, J., 2016. Afterslip and viscoelastic relaxation model inferred from the large-scale post-seismic deformation following the 2010 Mw 8.8 Maule earthquake (Chile), *J. geophys. Int.,* **205**(3), 1455–1472.
Kong, A., 1992. A note on importance sampling using standardized weights, Technical Report 348, Department of Statistics, University of Chicago.
Kong, A., Liu, J.S. & Wong, W.H., 1994. Sequential imputations and Bayesian missing data problems, *J. Am. Stat. Assoc.,* **89**(425), 278–288.
Koohkan, M.R. & Bocquet, M., 2012. Accounting for representativeness errors in the inversion of atmospheric constituent emissions: application to the retrieval of regional carbon monoxide fluxes, *Tellus B,* **64,** doi:10.3402/tellusb.v64i0.19047.
Kudo, T., Yamaji, A., Furumoto, M. & Nagao, T., 2001. Effective elastic thickness of island arc lithosphere under Japan, *Island Arc,* **10**(2), 135–144.
Kumar, U., Chao, B.F. & Chang, E. T.Y., 2020. What causes the common-mode error in array GPS displacement fields: case study for Taiwan in relation to atmospheric mass loading, *Earth Space Science,* **7**(11), e2020EA001159, doi:10.1029/2020EA001159.
Liu, X., Zhao, D. & Li, S., 2014. Seismic attenuation tomography of the Northeast Japan arc: insight into the 2011 Tohoku earthquake (Mw 9.0) and subduction dynamics, *J. geophys. Res.,* **119**(2), 1094–1118.
Loveless, J.P. & Meade, B.J., 2010. Geodetic imaging of plate motions, slip rates, and partitioning of deformation in Japan, *J. geophys. Res.,* **115**(B2), doi:10.1029/2008JB006248.
Lui, J. & Chen, R., 1998. Sequential Monte Carlo methods for dynamical systems, *J. Am. Stat. Assoc.,* **90,** 567–576.
Luo, H. & Wang, K., 2021. Postseismic geodetic signature of cold forearc mantle in subduction zones, *Nat. Geosci.,* **14,** 104–109.
Maggi, A., Jackson, J., McKenzie, D. & Priestley, K., 2000. Earthquake focal depths, effective elastic thickness, and the strength of the continental lithosphere, *Geology,* **28**(6), 495–498.
Mavrommatis, A.P., Segall, P. & Johnson, K.M., 2014. A decadal-scale deformation transient prior to the 2011 Mw 9.0 Tohoku-Oki earthquake, *Geophys. Res. Lett.,* **41**(13), 4486–4494.
Mazzotti, S., Dragert, H., Hyndman, R.D., Miller, M. & Henton, J.A., 2002. GPS deformation in a region of high crustal seismicity: N. Cascadia forearc, *Earth planet. Sci. Lett.,* **198**(1), 41–48.
Melosh, H.J. & Raefsky, A., 1983. Anelastic response of the earth to a dip slip earthquake, *J. geophys. Res.,* **88**(B1), 515–526.
Minson, S.E., Simons, M. & Beck, J.L., 2013. Bayesian inversion for finite fault earthquake source models I—theory and algorithm, *J. geophys. Int.,* **194**(3), 1701–1726.
Minson, S.E. *et al.*, 2014. Bayesian inversion for finite fault earthquake source models—II: the 2011 great Tohoku-Oki, Japan earthquake, *J. geophys. Int.,* **198**(2), 922–940.
Muto, J., 2011. Rheological structure of northeastern Japan lithosphere based on geophysical observations and rock mechanics, *Tectonophysics,* **503**(3), 201–206.
Nakagawa, H., 2009. Development and validation of geonet new analysis strategy (version 4), *J. Geogr. Surv. Inst.,* **118,** 1–8.
Nishimura, T., Sagiya, T. & Stein, R., 2007. Crustal block kinematics and seismic potential of the northernmost Philippine Sea Plate and Izu microplate, central Japan, inferred from GPS and leveling data, *J. geophys. Res,* **112,** doi:10.1029/2005JB004102.
Nolet, G., 2008. *A Breviary of Seismic Tomography,* Cambridge Univ. Press.
Ohzono, M., Yabe, Y., Iinuma, T., Ohta, Y., Miura, S., Tachibana, K., Sato, T. & Demachi, T., 2013. Strain anomalies induced by the 2011 Tohoku Earthquake (Mw 9.0) as observed by a dense GPS network in northeastern Japan, *Earth, Planets Space,* **64**(17), doi:10.5047/eps.2012.05.015.
Okada, T., Yaginuma, T., Umino, N., Kono, T., Matsuzawa, T., Kita, S. & Hasegawa, A., 2005. The 2005 M7.2 Miyagi-Oki earthquake, NE Japan: possible rerupturing of one of asperities that caused the previous M7.4 earthquake, *Geophys. Res. Lett.,* **32**(24), doi:10.1029/2005GL024613.
Oliver, D.S., Reynolds, A.C. & Liu, N., 2008. *Inverse Theory for Petroleum Reservoir Characterization and History Matching,* Cambridge Univ. Press.
Ozawa, S., Nishimura, T., Munekane, H., Suito, H., Kobayashi, T., Tobita, M. & Imakiire, T., 2012. Preceding, coseismic, and postseismic slips of the 2011 Tohoku earthquake, Japan, *J. geophys. Res.,* **117**(B7), doi:10.1029/2011JB009120.
Preisendorfer, R., 1988. *Principle Component Analysis in Meteorology and Oceanography,* Elsevier.
Resovsky, J. & Trampert, J., 2003. Using probabilistic seismic tomography to test mantle velocity-density relationships, *Earth planet. Sci. Lett.,* **215**(1), 121–134.
Sagiya, T., 2004. A decade of GEONET: 1994-2003, *Earth, Planets Space,* **56**(8), xxix–xli.
Sagiya, T., Miyazaki, S. & Tada, T., 2000. Continuous GPS array and present-day crustal deformation of Japan, *Pure appl. Geophys.,* **157,** 2303–2322.
Saltelli, A. & Annoni, P., 2010. How to avoid a perfunctory sensitivity analysis, *Environ. Modell. Softw.,* **25**(12), 1508–1517.
Sambridge, M. & Mosegaard, K., 2002. Monte Carlo methods in geophysical inverse problems, *Rev. Geophys.,* **40**(3), 3–1-3-29.
Snyder, C., Bengtsson, T., Bickel, P. & Anderson, J., 2008. Obstacles to high-dimensional particle filtering, *Mon. Wea. Rev.,* **136**(12), 4629–4640.
Socquet, A. *et al.*, 2017. An 8 month slow slip event triggers progressive nucleation of the 2014 Chile megathrust, *Geophys. Res. Lett.,* **44**(9), 4046–4053.
Sun, T. & Wang, K., 2015. Viscoelastic relaxation following subduction earthquakes and its effects on afterslip determination, *J. geophys. Res.,* **120**(2), 1329–1344.

Sun, T., Wang, K. & Iinuma, T., 2014. Prevalence of viscoelastic relaxation after the 2011 Tohoku-Oki earthquake, *Nature,* **514,** 84–87.

Talagrand, O., 1997. Assimilation of observations, an introduction, *J. Meteorol. Soc. Jpn.,* **75,** 191–209.

Tarantola, A., 1984. Inversion of seismic reflection data in the acoustic approximation, *Geophysics,* **49**(8), 1259–1266.

Tesauro, M., Kaban, M.K. & Cloetingh, S.A., 2013. Global model for the lithospheric strength and effective elastic thickness, *Tectonophysics,* **602,** 78–86.

Turcotte, D.L., McAdoo, D.C. & Caldwell, J.G., 1978. An elastic-perfectly plastic analysis of the bending of the lithosphere at a trench, *Tectonophysics,* **47**(3), 193–205.

van Dinther, Y., Preiswerk, L. & Gerya, T., 2019. A secondary zone of uplift due to megathrust earthquakes, *Pure appl. Geophys,* **176,** 4043–4068.

van Leeuwen, P.J., 2003. A variance-minimizing filter for large-scale applications, *Mon. Wea. Rev.,* **131**(9), 2071–2084.

van Leeuwen, P.J., 2009. Particle filtering in geophysical systems, *Mon. Wea. Rev.,* **137**(12), 4089–4114.

van Rijsingen, E.M., Calais, E., Jolivet, R., de Chabalier, J.-B., Jara, J., Symithe, S., Robertson, R. & Ryan, G.A., 2021. Inferring interseismic coupling along the Lesser Antilles Arc: a bayesian approach, *J. geophys. Res.,* **126**(2), e2020JB020677, doi:10.1029/2020JB020677.

van Dinther, Y., Künsch, H.R. & Fichtner, A., 2019. Ensemble data assimilation for earthquake sequences: probabilistic estimation and forecasting of fault stresses, *J. geophys. Int.,* **217**(3), 1453–1478.

Vening Meinesz, F., 1931. Une nouvelle methode pour la reduction isostatique regionale de l'intensite de la pesanteur, *Bull. Geod.,* **29,** 22–51.

Vossepoel, F.C. & van Leeuwen, P.J., 2007. Parameter estimation using a particle method: inferring mixing coefficients from sea level observations, *Mon. Wea. Rev.,* **135**(3), 1006–1020.

Walcott, R.I., 1970. Isostatic response to loading of the crust in canada, *Can. J. Earth Sci.,* **7**(2), 716–727.

Wang, K., Hu, Y. & He, J., 2012. Deformation cycles of subduction earthquakes in a viscoelastic earth, *Nature,* **484,** 327–332.

Wang, Z. & Zhao, D., 2005. Seismic imaging of the entire arc of Tohoku and Hokkaido in Japan using P-wave, S-wave and sP depth-phase data, *Phys. Earth planet. Inter.,* **152**(3), 144–162.

Watanabe, S., Ishikawa, T., Nakamura, Y. & Yusuke, Y., 2021. Co- and postseismic slip behaviors extracted from decadal seafloor geodesy after the 2011 Tohoku-Oki earthquake, *Earth Planets Space,* **73**(162), doi:10.1186/s40623-021-01487-0.

Wesson, R., Melnick, D. & Cisternas, M., 2015. Vertical deformation through a complete seismic cycle at Isla Santa María, Chile, *Nat. Geosci.,* **8,** 547–551.

Wikle, C.K. & Berliner, L.M., 2007. A Bayesian tutorial for data assimilation, *Physica D,* **230**(1), 1–16.

Yamagiwa, S., Miyazaki, S., Hirahara, K. & Fukahata, Y., 2015. After-slip and viscoelastic relaxation following the 2011 Tohoku-oki earthquake (Mw9.0) inferred from inland GPS and seafloor GPS/Acoustic data, *Geophys. Res. Lett.,* **42**(1), 66–73.

Yamanaka, Y. & Kikuchi, M., 2003. Source process of the recurrent Tokachi-oki earthquake on September 26, 2003, inferred from teleseismic body waves, *Earth Planet Space,* **55**(e21–e24),.

Yokota, Y. & Koketsu, K., 2015. A very long-term transient event preceding the 2011 Tohoku earthquake, *Nat. Commun.,* **6,** doi:10.1038/ncomms6934.